

Reply to the reports on manuscript AMT-2020-90

Thomas Trickl, October 26, 2020

The comments received are highly valuable. Indeed, shortening is reasonable. Since the paper was written over quite a few years the importance of some of the technical has changed. The focus must be on the most recent state of knowledge.

The development and testing of the system has undergone several stages, interrupted by waiting for new equipment when work for other projects was done by our small team. This is the reason why we just recently reached a technical and data-evaluation level to start routine measurements.

The text of the two reports are given in italics, the replies normal. A file with the changes marked is submitted as supplementary material.

Review 1:

We appreciate the particularly careful reading of our paper. This has been very helpful indeed!

This manuscript describes the development of a high-power Raman water vapor lidar deployed at a high-elevation site near Garmisch-Partenkirchen, Germany. Based on its somewhat heterogeneous content and style, the manuscript seems like the concatenation of several work efforts covering the period 2012-2019. It is long and very detailed, often too detailed, which makes it sometimes difficult to follow, and also makes the actual objectives unclear. For example, the abstract mentions an “existing” co-located DIAL (used for calibration), but this system has been out of operation since 2014. Another example is the multiple references to temperature measurements, including in the manuscript title. These measurements are separated from the water vapour system, as they are made with a Nd:Yag laser. They do not fit well in the present manuscript, which focuses on the high-capability water vapour measurements.

Our goal has been to describe the lidar system as a whole. The entire receiver design is made for water vapour, ozone and temperature. This must be explained. In particular, one chapter is devoted to characterizing the capability for temperature measurements. The Nd:YAG laser is part of the system, similar to current implementations of stratospheric ozone DIALs at several stations!!!

Of course, water vapour is our primary target and most of the paper is about H₂O. However, when the system was funded there was a strong demand also on T measurements by local groups.

The long T part in the title emerged from a discussion with the editor. Initially, the title was much shorter.

The DIAL was used in a demonstration of a side-by-side calibration of the Raman lidar. A new laser system for this DIAL is under development, but this development has proceeded slowly recently due the current lack of personnel, especially after my retirement. Emission was already observed for a much faster repetition rate of 100 Hz. The future use of the DIAL is promised in the conclusions.

Because of the level of detail and length, I strongly suggest that many sections of the manuscript be used as “Supplementary material”, and that the authors leave in the main manuscript only the critical steps that led to the instrument’s current configuration. The authors should add a discussion/conclusion on expectations in terms of future measurement contributions and strategic goals.

During the revision I tried to shorten the content as far as possible. I personally dislike “supplementary material” because this means additional downloading efforts for the reader. The length of paper is really not excessive.

A few statements about the future were added.

In regards to experimental development, the technical content is very important, and for that reason, should be published, assuming that Supplementary Material can be separated from the main manuscript. I therefore recommend publication after major revisions.

Suggestions for major revisions:

1) For water vapor there are only 4 measurement nights shown (4/25/2013, 7/1/2015, 7/19/2018, and 2/5/2019), including only 1 comparison with CFH. For temperature, there is only one night shown. To my opinion, this is not enough to characterize the performance of an instrument, especially when the study period spans 7 years. I strongly suggest that the authors show more profiles and/or statistics (e.g., mean differences aggregated from all available measurement nights), and possibly a climatology. Also I strongly suggest that the authors show one or more curtain plots showing the shortterm (overnight) water vapor changes as a function of time and altitude. As the authors claim in the manuscript, this is one of the strengths of lidar, yet they have not shown any examples of it.

The measurements were selected from a much larger number starting in 2018 as specified in the first paragraph of Sec. 6.1. All these profiles look reasonable. The examples were chosen to show the performance under different conditions, such as high and low noise or different situations and methods for the calibration. An introductory remark was added.

This is not a paper on system validation: It is paper on the system development and testing. A full-size validation exercise has been out of scope and would require additional funding. Unfortunately, the CFH team was present just for two days, the second day being devoted to cloud cases!

2) Below are three sections which I believe are too detailed, and therefore fit better as “Supplementary material”. They can be replaced in the main manuscript by shortened paragraphs or sentences that summarize the “take-home” message and provide a more fluid read:

- Sections 2.2 and 2.3, and corresponding figures 2, 3, 4, 5

These sections are now shortened and two figures were removed. There are paragraphs that were important at some time in the project, but no longer matter. We spent significant time on these studies and on buying and testing new components which explains the amount of detail! Now, just the outcome of these efforts is briefly described (e.g., spectral behaviour, Raman scattering). The chapter on stimulated Raman scattering now just explains why this approach was abandoned, an important message for future efforts elsewhere.

- Sections 3.3., 3.4, and corresponding figures 10, 11

We believe that these section are key sections and should not serve as supplementary material. This is a paper on the system development and testing, and this kind of information is the basis for the understanding of the results discussed. However, considering the rather complete description in our companion paper on our tropospheric ozone DIAL systems, some details were dropped.

-Section 4.4., and corresponding Fig 12 (also see my comment on this section further below)

Other major comments:

Section 4.4, and Fig 12:

This section does not bring important information to the paper, besides showing the lidar sensitivity to H₂O in the UTLS. It can be removed from the manuscript. If kept in the manuscript, it should be included earlier (e.g., in the introduction) as a mean to state the problem.

This chapter is needed to judge the results (see discussion section). In the introduction it would be too early. It is short anyway.

Section 5 (Calibration):

Using the DIAL as a calibration source is a very interesting approach. However, it is mentioned that the DIAL has been inoperative since 2014. This section does not provide any other information on how the Raman lidar has been calibrated since then (including accuracy), and most importantly, what is the timeline to use the DIAL system again for calibration (if it will ever be used again).

The laser development for the DIAL looks very promising, and it is planned to complete it. This is clearly stated in Sec. 5 and in the conclusions. I added a paragraph on the sondes to Sec. 5.

Minor comments:

P3/12, Radiosonde weakness: Outdated literature. RS92 has been replaced by RS41, with better performance in the UTLS

Our results show that RS 41b does not mean any improvement at all in the lower stratosphere. Maybe the sonde itself is better than RS 92. However, the corrections for RS 92 seem to be better. As mentioned in Sec. 6 there is also a wet bias for low RH values in the troposphere that does not exist in the RS 92 profiles. I removed the sentence on the RS 92 sonde: Too much detail in the introduction!

P3/14, CFH: Use full instrument name Cryogenic Frost-Point Hygrometer

Done, next occurrence of CFH on P. 3 also modified,

P3/18, “Raman scattering is a background-free method”: this is an awkward expression. Please rephrase.

This is an expression frequently used in laser-based analytics. However, I slightly modified it.

P3/133, DIAL accuracy: Proper reference should point to HITRAN 2008. Cited references mention 2% and 3.2%. Please clarify where the figure “1% or less” comes from.

This comes from our own validation exercises in the papers cited! Also a comparison with HITRAN is made there. The spectroscopic data of Ponsardin and Browell, used for the calibration of our DIAL, are obviously more accurate.

P3/137, “355 nm” and p4/12: The single temperature profile shown in this manuscript comes from a Nd:Yag, not the Excimer laser described for water vapour. This distinction makes the inclusion of temperature in this manuscript somewhat off-subject.

Numerous temperature profiles were retrieved from measurements with the Raman-shifted excimer which will be in part presented by L. Klanner in her thesis.

P7/131 and 133: Should refer to fig 7, not fig 6.

Thank you! The numbers have changed anyway due to discarding two figures.

P13/18, “multiplying the backscatter signal : : . by the square of distance r”: If both the N₂ and H₂O detectors are triggered simultaneously, there is no need for range correction at all, which makes this sentence out of context. Please clarify or modify the sentence.

This sentence is correct: The quantity discussed in this statement is the number density, for me the primary target quantity. The statement makes clear that (if ozone is neglected) the data evaluation is simple and robust. However, for the test period presented here we preferred to avoid an ozone correction due to the problems with the generation of 353-nm radiation. I added a remark further below.

P13/115, “the influence of ozone exactly cancels because the transmitted wavelength is the same”: This is an incorrect statement. There is a slight extinction differential associated with the returned signals (after backscatter). However, it is expected to be small for most of the troposphere because absorption at 332 and 347 nm is weak. It can however impact the measurement in the LS as ozone becomes more abundant. Please provide estimate of the ozone interference (this is quantifiable)

Thank you for this remark! Indeed, a small deviation of exists in the N₂ signals that reached almost 2 % at 20 km, estimated from the ozone climatology of Hohenpeißenberg for the months with maximum ozone. A sentence pointing this out was added. The ozone influence in the H₂O channel is lower by one order of magnitude.

P13/118, “data are collected at 51.2 ns per bin”: Is the laser pulse length 80 ns? What are the implications of such a long pulse on data sampling?

Not more than 2 bins! In the UTLS smoothing is applied. I think we should not comment on this issue. For near-field data the exact position of the zero point matters indeed.

P13/139, “The role of aerosols is limited to extinction in a Raman lidar”: Not entirely true. Fluorescence has been observed as well (e.g., Immler et al., 2005). Please modify sentence accordingly and discuss its impact. For example, a strong, widespread and sustained episode of bio-fluorescence was observed at Northern mid-latitudes during Fall 2017 after the so-called Chisolm PyroCb event. Did the IMK-IFU lidar observe it? Please clarify/expand.

The work of Franz Immler and Jens Reichardt is well known to me, thank you for reminding me. Our measurements were all made during clear nights without aerosol over many hours to allow for playing with the settings. I added two statements.

P17 and fig 14: These results have been shown before at several occasions. The lengthy discussion is unnecessary

These results were to some extent explained in the 2017 ILRC proceedings. I think it is not fair just to refer to that paper. The figures are presented now in a much better way, including smoothing, and show more detail. The calibration figure in the ILRC paper is not repeated (now cited).

I took this example because since it shows what can be achieved under worst-case conditions, i.e., with an open polychromator entrance slit with strong lunar background, that stratospheric water vapour can be resolved even under these conditions. In addition, there is good agreement with an RS 92 sonde (in contrast to that with RS 41 in the other examples). From a scientific point of view, the case is interesting because of a very dry layer, which indicates that the distributions do not look the same all the time in the stratosphere.

The section is not really long. Some modifications were made.

P18/119, "not as reliable": What do the authors mean by "not as reliable"? What is the physical basis for such statement?

I modified that part.

P18/120, "We speculate that this is due to a change in sonde type from RS 92 to RS 41": RS41 is expected to be more accurate than RS92 in the LS. Please justify this statement that seems to go against current general thinking about the latest RS41 radiosondes

We give several comparisons in this section suggesting a non-ideal behaviour of RS 41. The statement about our tropospheric studies underlines that there are some issues with RS 41 that do not exist for RS 92. I informed the German Weather Service about this. Maybe the RS 41 sonde itself is better than RS 92, but adequate corrections are missing.

P19, section 6.2: The entire section, together with Fig. 21, is of poor scientific or technical interest. I would like to suggest to just remove it altogether. One of the correlative curves is extrapolated, which has no scientific value, and the apparent agreement between the lidar and correlative densities is fully expected with a figure of such aspect ratio (showing 10 orders of magnitude on the X-axis!). If any relative density comparison really must be shown, please use a ratio to the US standard atmosphere density for better visibility.

From the remarks I conclude that not the entire section 6.2 is meant, just Fig. 21 and its description. This is an exclusively technical paper. The scientific importance is described in the introduction. In Fig. 21 (19), we give the best example for the system performance, the scale extending out to 120 km. with average counts below 1. It is generally the habit in lidar papers to present examples of the raw data.

Indeed, the NCEP data end at 50 geopotential km. This was respected in Fig. 22. Here, the extrapolation was made to guide the eyes. I remove the extrapolation.

It is a good suggestion to show that ratio, but the details can be also (and better) seen in Fig. 22.

Some adjustments were made.

P21/125, "The temperature measurements : : : were quite successful": Only one temperature profile is shown to support this conclusion. Please modify to mitigate this statement, or include more temperature comparisons to support it.

Done.

Syntaxing and formatting issues:

p1/123: UTLS

Removed.

p1/133: Missing verb

"shows" added.

p1/136: Syntax

Changed.

p2/136:: Add "water vapor" between "ground-based" and "lidar"

Added.

p17/138, “background signal”: missing verb

“and” removed.

p18/124: Syntax

Second “5” replaced by “6”.

p27: Trickl/Wilson references misplaced

The paper co-authored by K. Wilson is not misplaced. Also “(1998)” refers to a different paper. However, I introduced 2010a and 2010b.

p28: Two conflicting 2020 references for Trickl 2020

Also here I introduced a and b.

Figures:

A lot of figure captions contain excessive narrative discussion. Please move those to the main text. Fig 9 caption: way too long and detailed. Most of it should be kept in the main text or put together in a table

I found several sentences or phrases that could be removed, in particular narrative ones. The captions now explain just what is seen in the figures (e.g. the abbreviations), which is the habit.

Figure 21 caption: too long. Keep discussion in the main text.

Indeed, the text is narrative: Changed!

Review 3:

This manuscript describes a high-power Raman lidar system has been installed at Schneefernerhaus (Garmisch-Partenkirchen, Germany) at 2675 m a.s.l., at the side of an existing wide-range differential-absorption lidar (DIAL). An industrial XeCl laser was modified for linearly polarized single-line operation at an average power of about 180W. This high power and a 1.5-m-diameter receiver allow us to extend the operating range for water-vapour sounding to 20 km for a measurement time of just one hour, at an uncertainty level of the mixing ratio of 1 to 2 ppm. The lidar was successfully validated with a balloon-borne cryogenic frost-point hygrometer (CFH). In addition, temperature measurements to altitudes around 87 km were demonstrated for one hour of signal averaging. The system has been calibrated with the DIAL, the CFH and radiosondes.

General Comments:

In general this manuscript describes the lidar system in an immense detail. At times it can get confusing as to which lidar system or which component is being described.

The laser section was shortened as indicated in the first reply (see above).

Consider alternate word choice for the term ‘powerful’ in the title or ‘stronger’ in the abstract, they are both ambiguous.

The title is already rather long. It does not make sense to add complexity. “Powerful” is underlined by the measurement time of 1 h. The rest is explained in the paper.

“stronger” is explained by the vertical resolution specified in the first part of the sentence. However, I deleted the second part because the message is trivial.

The introduction is not logically presented as many key words are missing from sentences and there is no consistent message. Consider adding a key figure or illustration that better gives the reader a perspective on where the lidar would help understand either trends or process studies (or both). There are statements without adequate referencing. This can and should be related back to the atmospheric case study to better support the importance of the vertical lidar profile.

Which key words are missing?

The introduction is also quite long and some is described in the authors previous 2008 work (<https://doi.org/10.1364/AO.47.002116>). Consider shortening or directing the reader to this publication for more details regarding the DIAL.

The length of the introduction is rather typical in comparison with other full-size papers. It covers a reasonable number of aspects relevant for wide-range sounding of water vapour.

I do not understand the remark about the DIAL at all: That paragraph is already short and the reader is lead to the relevant papers as demanded.

In general the lidar description has very useful information but is organized as one would take field notes. There needs to be some explanation as to why many of these parameters are important. It's also not clear that the thin film polarizer or Raman cell (SRS) are actually used in the experiment as there is no final outcome described. There are too many varied parameters (focal length, rep rate, input power, cell length) for the reader to come away with any conclusion.

We removed complexity. The Raman-shifting chapter was shortened since Raman shifting was abandoned. It was not completely removed since whoever wants to build such a system should know that this approach has its limits.

Additional water vapor lidar references include : [https://doi.org/10.1175/1520-0426\(1995\)012<1177:ACOWVM>2.0.CO;2](https://doi.org/10.1175/1520-0426(1995)012<1177:ACOWVM>2.0.CO;2)

This and other papers are known to me. Here, we just cite lidar systems for with demonstrated a range exceeding the tropopause was demonstrated (LS in UTLS).

Technical Comments:

P1L23 – disregard the first use of UTLS

Done.

P1L26-29 – provide further references for these statements

There is a host of literature on transport into the UTLS region. Some of it was discussed in our STT paper 2014. Most of the investigations a related to airborne measurements, especially by the MOZAIC and CARIBIC teams. Because of the typical flight levels the information is mostly limited to the tropopause region, where a “mixing layer” exists. In our aerosol measurements (Trickl et al., 2013) we frequently see aerosol contributions around the tropopause, related to moderate volcanic eruptions, fire plumes or desert dust.

Transport farther into the stratosphere is reported for aerosol observations (e.g., Fromm et al. in various publications). Immler et al. (2005) show one case of fluorescing aerosol that was very likely lifted to altitudes beyond the tropopause region in a WCB outflow. However, the sensitivity of that

lidar for water vapour in the stratosphere was limited, also because of the co-incident fluorescence peak.

Transport to the tropopause region remains interesting. Transport to altitudes beyond the UTLS seems to be an open territory. In any case: this paper is fully technical and the description of scientific issues should remain limited. I added a few more references on key papers on the chemical composition of the UTLS layer.

P1L29 – Write out NCEP in first use

Done.

P3L28 – Is the lidar used in daytime or during nighttime? Or DIAL during the day and Raman system during the night?

I added “during night-time” to the sentence about the Raman lidar. It is obvious that the DIAL must also be operated during night-time to achieve a calibration, in addition to day-time sounding.

Figure 1/3 – can these be combined?

I do not see a reason for this. This would blow up the caption.

Figure 13: How is the WV calibration calculated for this night? For instance, it looks as a scaled factor could be applied to the WV profile. What is the difference at 2km caused by?

Calibration of course means determining an average scale factor. As pointed out this was done at higher altitudes where the influence of the artefact mentioned was less severe. The result looks acceptable also at lower altitudes.

2 km: As mentioned the measurements for the two lidar systems were not made exactly at the same time. Changes in humidity may occur at very short time scales (Vogelmann, 2011). I added a statement concerning this.

Consider reducing the number of individual water vapor comparison profiles or make an aggregate summary plot. How many measurements of WV are there with the new system? Feb 2019 is the most compelling of the case studies as an excellent comparison with the CFH.

Here, we just give a description on the system development and some idea about the performance. The figures have been chosen from the aspects of the limitations of the comparison with sondes and the necessity for DIAL-based calibration. I think the selection of figures is adequate.

Conclusions: How frequent are the temperature measurements? Is this system automated?

This system will soon be automated or, at least, will be operated under remote control via the internet, as indicated in the text. Most options have been tested. A problem is the photon-counting systems that, for reliable starts of the measurements, must be operated via mouse click (on a remote computer). The NDACC aerosol measurements have been performed at UFS in this way in recent years.

A statement was added to the conclusions.

1 **A powerful lidar system capable of one-hour measurements of**
2 **water vapour in the troposphere and the lower stratosphere as**
3 **well as the temperature in the upper stratosphere and mesosphere**

4 Lisa Klanner¹, Katharina Höveler¹, Dina Khordakova², Matthias Perfahl¹, Christian Rolf²,
5 Thomas Trickl¹, Hannes Vogelmann¹

6 ¹Karlsruher Institut für Technologie, Institut für Meteorologien und Klimaforschung (IMK-IFU),
7 Kreuzeckbahnstr. 19, D-82467 Garmisch-Partenkirchen, Germany

8 ²Forschungszentrum Jülich, IEK-7, Wilhelm-Johnen-Straße, 52425 Jülich, Germany
9

10 *Correspondence to:* Dr. Thomas Trickl, e mail: thomas@trickl.de, Tel. 0049-8821-50283

11 **Abstract.** A high-power Raman lidar system has been installed at the high-altitude research station
12 Schneefemerhaus (Garmisch-Partenkirchen, Germany) at 2675 m a.s.l., at the side of an existing wide-range
13 differential-absorption lidar (DIAL). An industrial XeCl laser was modified for linearly polarized single-line
14 operation at an average power of about 180 W. This high power and a 1.5-m-diameter receiver allow us to
15 extend the operating range for water-vapour sounding to 20 km for a measurement time of just one hour, at an
16 uncertainty level of the mixing ratio of 1 to 2 ppm. This was achieved for a vertical resolution varied between
17 just 0.2 and 0.6 km in the stratosphere ~~and could be improved for stronger smoothing~~. The lidar was successfully
18 validated with a balloon-borne cryogenic frost-point hygrometer (CFH). In addition, temperature measurements
19 to altitudes around 87 km were demonstrated for one hour of signal averaging. The system has been calibrated
20 with the DIAL, the CFH and radiosondes.

21 *Key words:* Lidar, Raman lidar, water vapour, temperature

22 **1 Introduction**

23 Water vapour ~~UTLS~~ in the upper troposphere and lower stratosphere (UTLS) is the key factor controlling how
24 much thermal infrared radiation escapes from the atmosphere into space (e.g., Kiehl and Trenberth, 1997;
25 Schmidt et al., 2010; Lacis et al., 2013). In a warmer climate the atmosphere takes up more water vapour from
26 the sea surface. However, this increase could be counteracted by additional cloud formation and precipitation.
27 Also vertical exchange processes could change in a warmer climate (Trickl et al., 2010a; 2020a). Water vapour
28 trends in the troposphere derived from observations are discussed in literature. Paltridge et al. (2009) report
29 negative trends for the period 1973 to 2007 at all free-tropospheric altitudes in NCEP ([National Centers for](https://www.ncep.noaa.gov/)
30 [Environmental Prediction, https://www.ncep.noaa.gov/](https://www.ncep.noaa.gov/)) re-analysis data, in particular in the upper troposphere,
31 in contrast to the expectations from climate modelling. Other studies show at least regionally positive trends
32 (Ross and Elliott, 2001; Mieruch et al. 2008; Chen and Liu, 2016). However, they evaluate columnar quantities
33 that are dominated by the moist boundary layer where thermal radiation is trapped by water vapour anyway. In
34 the lower stratosphere, the Boulder series ~~shows~~ a trend reversal from positive to negative occurred around 2000
35 (Hurst et al., 2011), but the pronounced positive trend during the early phase since the late 1980s is not
36 confirmed for other locations (Solomon et al., 2010; Hegglin et al., 2014).

37 Due to ~~its-the~~ role of water vapour as the most important greenhouse gas the optimization of high-accuracy,
38 range-resolved vertical sounding instrumentation covering the entire free troposphere and the lower stratosphere

1 has become more and more important during the past two decades (Kämpfer et al., 2013). All the most
2 commonly used sensors used for routine measurements have limitations. Operational radiosondes have been
3 greatly improved within the troposphere in recent years, but deficiencies exist in the very cold tropopause region
4 and the lower stratosphere where the sensors exhibit slow response and low sensitivity (Miloshevich et al., 2006;
5 Vömel et al., 2007a; Steinbrecht et al., 2008; Kämpfer et al., 2013). Balloon-borne cryogenic [frost-point](#)
6 [hygrometers](#) (CFH) ~~sondes~~ (Vömel et al., 2007b; 2016; Kämpfer et al., 2013; Hurst et al., 2016) and Lyman
7 alpha hygrometers (Kley and Stone, 1978; Weinstock et al. 1990; Khattatov et al., 1994; Hintsä et al., 1999;
8 Zöger et al., 1999; Kämpfer et al., 2013), though being highly accurate, are rarely used in dense routine
9 measurement programmes due to their elevated costs. Ground-based microwave radiometers have an excellent
10 temporal coverage, but their application is limited to the lower and middle troposphere (Westwater, 1978; Han
11 and Westwater, 1995; Solheim and Godwin, 1998) and altitudes above 20 km (Nedoluha et L., 1997; Deuber al.,
12 2004; 2005; Kämpfer et al., 2013) with somewhat limited vertical resolution. The value of satellite-borne
13 measurements (Kämpfer et al., 2013) is limited by the considerable spatial averaging that results in a loss of
14 information due to the high variability of water vapour even in the lower stratosphere (Zahn et al. 2014), but can
15 yield reasonable averages and global coverage (e.g., Solomon et al., 2010).

16 There is just one long quantitative ground-based sounding series of stratospheric water vapour, obtained with the
17 Boulder balloon-borne ~~eryogenic frost-point hygrometer~~ [CFH](#) (Scherer et al., 2008; Hurst et al., 2011). These
18 measurements have been carried out since 1980 at intervals of about one measurement per month. Because of the
19 considerable variability of water vapour up to at least the UTLS more frequent measurements with good vertical
20 resolution are desirable (Müller et al., 2016). This variability is caused to a major extent by transport-induced
21 patterns. Injections of water vapour into the stratosphere occur not only in the tropics (Rosenlof, 2003), where
22 also freeze-drying has been claimed to matter (see, e.g., the discussions by Peter et al. (2003), Luo et al. (2003),
23 Jensen et al. (2007) and Zahn et al. (2014)), but also in the jet-stream regions (Stohl et al., 2003; and references
24 therein). ~~Troposphere-to-stratosphere transport (TST) in vicinity of the jet streams, e.g., by overshooting~~
25 ~~moist~~ [Warm conveyor belts \(WCBs\) can lift moist polluted air from the boundary layer to the tropopause region](#)
26 [\(Stohl and Trickl, 1999\). warm conveyor belts](#) ~~Overshooting WCBs can even transfer water vapour into the lower~~
27 [stratosphere \(WCBsLS; Stohl, 2001\) can be expected to yield a significant contribution \(Stohl, 2001; Zahn et al.,](#)
28 [2014\)](#), although possibly diminished by dehydration due to cirrus-cloud formation (cirrus clouds being almost
29 ubiquitous in WCB air probed by our lidar systems). [Most investigations related to this topic have been limited](#)
30 [to airborne measurements of the chemical composition of the tropopause region \(e.g., Pan et al., 2007; Gettelman](#)
31 [et al., 2011; Zahn et al., 2014\)](#). It is reasonable to assume that water vapour transported into the ~~lower~~
32 [stratosphere \(LS\)](#) by TST is an important target for vertical sounding [of H₂O with enhanced temporal density](#).

33 ~~Also~~ ~~†~~ The opposite mechanism, stratosphere-to-troposphere transport (STT), is much more important than
34 previously thought, [at least](#) in Central Europe after some increase over several decades (Trickl et al., 2010a;
35 2020a). Growing STT can contribute to a lowering of the tropospheric humidity.

36 Lidar-based measurements have the potential of good temporal and vertical resolution and are, therefore,
37 attractive for resolving transport-related concentration changes. However, the use of lidar systems for water
38 vapour implies a major challenge due the strong decrease of both the backscatter signal and the water-vapour
39 concentration with altitude. Despite the problems related to the extreme signal dynamics the NDACC (Network
40 for the Detection of Atmospheric Composition Change) lidar working group has strongly advocated to develop
41 powerful ground-based [water-vapour](#) lidar systems with UTLS capability, with focus on the Raman lidar
42 technique. Several Raman lidar systems have already reached a reasonable UTLS performance (Congeduti et al.,

Trupdwluh#hijhvwhoow

1 1999; Whiteman et al., 2010; Dionisi et al., 2012; Leblanc et al., 2012; Dionisi et al., 2015, Vèrèmes et al.,
2 2019). Whiteman et al. (2010), Leblanc et al. (2012) and Vèrèmes et al. (2019) demonstrated vertical ranges
3 extending to more than 20 km a.s.l. for averaging over many hours.

4 The most important detection barrier in the lower stratosphere is the very small mixing ratio of water vapour of 4
5 to 5 ppm (e.g., Hurst et al., 2011). In principle, this would require a highly sensitive approach. Measurements of
6 molecules in a range far below one part per trillion with respect to normal conditions can be achieved in the
7 laboratory even under restrictive conditions (e.g., Trickl and Wanner, 1983; Trickl et al., 2010b). However, a
8 fluorescence lidar approach cannot be used for atmospheric H₂O because it electronically absorbs in the vacuum
9 ultraviolet spectral region and undergoes photo-dissociation as concluded from the diffuse bands (e.g., Yoshino
10 et al., 1997). As a consequence, lidar measurements of H₂O in the lower atmosphere are restricted to the
11 differential absorption lidar (DIAL) and Raman scattering methods. The detection sensitivity and the range of
12 the DIAL method is limited by the signal noise of the absorption measurement. Raman scattering is the least
13 sensitive approach. However, night-time Raman scattering is a so-called background-free method. Thus, the
14 sensitivity for water-vapour-signal can, in principle, be driven to any level by enhancement of the laser power
15 and the diameter of the receiver, as long as allowed by financial or technical restrictions. Very importantly, a
16 Raman lidar can be operated at wavelengths for which absorption in the atmosphere is negligible.

17 For a Raman lidar calibration with an external source is an important issue: The optical transmission data of a
18 Raman lidar and the Raman scattering cross sections cannot be determined with sufficient accuracy. In addition,
19 a degradation of the components must be taken into consideration. Thus, a trace-gas Raman lidar routinely
20 operated over an extended period of time must be repeatedly calibrated with external references and the stability
21 of the calibration must be verified. Mostly, radiosonde measurements are used as reference (e.g., Leblanc and
22 McDermid, 2008; Dionisi et al., 2010), but also calibration with H₂O column measurements are reported (Barnes
23 et al., 2008; Vèrèmes et al., 2019). The Vaisala RS 92 radiosonde operationally used by weather services for
24 many years features a high accuracy level in the troposphere (Miloshevich et al., 2006; Vömel et al., 2007a;
25 Steinbrecht et al., 2008). However, the Raman lidar systems are not necessarily located at routine balloon
26 sounding stations. Even for on-site sonde launches the sondes usually rapidly drift away from the lidar which
27 frequently results in discrepancies due to the high spatial variability of water vapour (Vogelmann et al., 2011;
28 2015). Infrequent comparisons with sondes necessitate additional performance control such as built-in lamps
29 (Dionisi et al., Leblanc and McDermid, 2008; 2011; 2012; Whiteman et al., 2011) or monitoring the radiation
30 backscattered from air or nitrogen.

31 At Garmisch-Partenkirchen, we first concentrated on the differential-absorption-lidar (DIAL) technique for
32 measuring free-tropospheric water vapour (Vogelmann and Trickl, 2008; Trickl et al., 2013-2016; 2020a). This
33 system has the great advantage of a good daytime performance. In recent years a high-power Raman lidar has
34 been built that extends the range of the DIAL into the lower stratosphere during night-time with a data-
35 acquisition time of just 1 h. Both systems are operated side by side at the Schneefernerhaus mountain station
36 (UFS, Umweltforschungsstation Schneefernerhaus, 47° 25' 00'' N, 10° 58' 46'' E) at an altitude of 2675 m,
37 which offers the possibility of direct and accurate calibration of the Raman lidar. The DIAL has been thoroughly
38 validated and is free of bias at an uncertainty level of 1 % of average concentrations or less (Vogelmann, et al.,
39 2011; Trickl et al., 2016). Both system probe the same atmospheric volume and can be very reliably compared
40 up to about 8 km where the DIAL data start to become noisy.

1 The large system allows us to make temperature measurements up to the mesosphere based on an established
2 approach for inverting the Rayleigh backscatter signal for 355 nm (Hauchecorne and Chanin, 1980). In this way,
3 not only the primary green-house gas, but also the most important climate parameter is provided.

4 In this paper we report the development and the current state of the Raman lidar, before the beginning of routine
5 measurements. We describe the steps to achieve up to 180 W of linearly polarized and single-line output from a
6 modified industrial xenon-chloride laser (308 nm) (Sect. 2), and the development of the far-field receiver
7 receiver featuring a primary mirror with a diameter of 1.5 m (Sect. 3). Parallel to the ozone DIAL at IMK-IFU
8 (Trickl et al., 2020b) a significant step forward in signal processing was made. The highly satisfactory lidar
9 performance is demonstrated by examples of 1-h atmospheric measurements, also including a first demonstration
10 of a temperature measurement up to 87 km (Sects. 4 and 6). Finally, conclusions and suggestions for upgrading
11 the lidar are made (Sect. 7).

12 2 Laser System

13 2.1 General Description

14 Figure 1 gives an overview of the transmitter section of the new UFS Raman lidar system in the rear part of the
15 lidar laboratory (see also Table 1). The transmitter consists of a high-power laser, a 2.5:1 cylindrical beam
16 expander to achieve a less intense 40×40 mm² quadratic beam (f = 100 mm – f = 250 mm combination,
17 transmittance T = 0.9985 % per lens), a hydrogen Raman shifter and a motorized (Astro System Austria, ASA)
18 beam steering mirror (not shown). The 0.5-m-diameter beam-steering mirror sending the radiation into the
19 atmosphere is located in a vertical emergency exit shaft outside the laboratory. All dielectrically coated optics, in
20 particular the large-diameter mirrors, were supplied by Laseroptik G.m.b.H. unless explicitly stated differently.

21 The efficiency of Raman scattering scales as λ^{-4} and, thus, is the highest in the ultraviolet (UV) spectral region.
22 Here, the by far most powerful radiation sources are excimer lasers. The radiation source used in our system is a
23 big XeCl laser system with a power of 350 W (pulse energy 1 J, repetition rate 350 Hz, pulse length 80 ns) in
24 energy-stabilized mode of operation that is normally used for industrial applications (Coherent Göttingen
25 (formerly: Lambda Physik), model Lambda SX 350C, size (l×w×h) = 2.500 m × 0.850 m × 1.925 m). The very
26 high power of this laser system is much more important than the single-pass absorption loss in stratospheric
27 ozone at the operating wavelength of 308 nm (Sect. 4.4). An ozone correction can be provided by a DIAL
28 approach with an “off” emission at 353 nm (stimulated Raman shifting the laser radiation in H₂) or at 355 nm
29 (frequency-tripled Nd:YAG laser).

30 The laser was transported to UFS by a cogwheel train of Zugspitzbahn A.G. There, it could be lifted to the 7th
31 floor of the building with the large elevator of UFS and then to the 8th floor with two pulleys, after removing the
32 stairs.

33 As a consequence of its primarily industrial application, the laser system is operated under computer control
34 providing energy stabilization and numerous safety features. This is highly helpful for the planned automatic
35 operation of the lidar system. However, a high beam divergence of nominally 1 mrad and 4 mrad in two
36 perpendicular transverse orientations, random polarization and a three-line spectrum as shown in Fig. 2 are
37 insufficient for the requirements of the lidar. Therefore, an approach had to be found for overcoming these
38 disadvantages, considering the dangerous power level of this laser.

39 For our lidar concept a linearly polarized narrowband radiation is needed. Injection seeding with a XeCl master
40 oscillator with these properties was the premier choice because this could have resulted in maintaining high
41 average power. However, this idea was given up because of the manufacturer pointed out that there was no easy

Irupdlhu#ihjvhvhoow

1 way of synchronization because of the specified 25- μ s pulse-to-pulse jitter of the big laser, and because of the
2 considerable additional complexity and costs.

3 Instead, an intra-cavity solution was chosen. The resonator was stretched as shown in Fig. 3. The intra-cavity
4 laser beam is first converted to an approximate squared cross section with another 2.5:1 cylindrical telescope in
5 order to reduce the intensity in the new rear section. It is then fed through a Brewster-angle thin-film polarizer
6 (transmittance 96 %) and a custom-made 70-mm-diameter Fabry-Perot etalon with 0.10 mm plate distance (SLS
7 Optics Ltd.; $R = 54\%$, $T_{\min} \approx 7\%$, $T_{\max} = 95.4\%$) to reach the 75-mm-diameter end mirror. The large diameter
8 of the etalon is expected to provide strong reduction of ablation of material by scattered UV radiation and the
9 resulting ageing of the etalon plates. The chosen plate distance sets the free spectral range exactly to twice the
10 wavelength difference between the two groups of emission lines in Fig. 2. When setting the transmission
11 maximum to the short-wavelength component (307.955 nm; all wavelengths in this paper are specified for
12 vacuum) the gain at the wavelength pair around 308.2 nm is suppressed, despite the residual transmittance of
13 about 7 %. Just the direct first-pass forward emission estimated by the manufacturer to about 7 mJ cannot be
14 avoided.

15 The beam divergence with our long cavity was smaller than that determined by the manufacturer. We measured
16 a burning spot of $2.0 \times 1.2 \text{ mm}^2$ generated on a metal plate by focussing with ~~the a~~ $f = 2.0\text{-m}$ lens in front of the
17 Raman shifter, corresponding to a divergence of $1.0 \times 0.6 \text{ mrad}^2$. After the 5:1 beam expansion the beam
18 divergence is 0.2 mrad or less, an important prerequisite for ensuring a moderate size of the focal areas in the
19 very large receiver and its polychromator. As explained further below the final focal length is 1.75 m, resulting
20 in a slightly better-collimated beam.

21 ~~Three $43 \times 43 \text{ mm}^2$ sand-blasted square apertures were inserted into the extended rear part of the cavity. In this~~
22 ~~way damage of components by reflections caused by accidentally rotating the etalon beyond the needed angular~~
23 ~~range is avoided. This can become a serious problem at a high repetition rates.~~

24 2.2 Laser Testing

25 *General Remarks*

26 Despite the pronounced intra-cavity losses after multiple passes through the laser cavity the maximum pulse
27 energy achieved at repetition rates below 100 Hz is about 0.75 J. We explain this by fresh gain generated all
28 along the 80 ns of laser emission and by 92 % of the amplified energy being emitted after each round trip. Thus,
29 the losses do not matter similarly as in a cavity with higher reflectance of the output mirror.

30 *Emission Spectrum*

31 ~~For spectral analysis we built a 6.15-m grating spectrograph with spare $f = 250 \text{ mm}$ cylindrical lenses of the laser~~
32 ~~cavity, a thin adjustable slit (OWIS) and a 1800 lines/mm grating, and a CCD camera (OPHIR) for recording the~~
33 ~~spectrum. The spectrograph was used in second order, the third and higher orders not being detectable. The~~
34 ~~spectral resolution was reasonable, but lower than that in Fig. 2 which was measured by Coherent in a high~~
35 ~~grating order. During these test measurements the polarizer was not yet installed.~~

36 ~~We first horizontally rotated the etalon with a perceivable vertical tilt angle. With this setting single line~~
37 ~~emission was achieved over a wide spectral range even exceeding that of the lines in Fig. 2, but with changing~~
38 ~~pulse energy. When the etalon was oriented perpendicularly to the laser beam the full emission spectrum was~~
39 ~~seen (lower panel of Fig. 4). We then slightly tilted the etalon vertically to the next power minimum and tuned it~~
40 ~~just horizontally. The spectral composition changed as a function of the angle and the pulse energy could be~~

1 optimized on each of the two peaks. The upper panel of Figure 4 shows an example for maximized emission on
2 the short wavelength component for a repetition rate of 300 Hz, and, after the end of this measurement, another
3 one for 50 Hz without etalon for spectral calibration.

4 ~~The contribution of the longer wavelength doublet for an optimum etalon angle is less than 0.5 %. This value is~~
5 ~~in reasonable agreement with the 7 mJ of initial forward emission mentioned above, considering that almost one~~
6 ~~half of this weak broadband emission goes into the correct wavelength component (Fig. 2). Towards higher~~
7 ~~wavelengths a rising background (presumably from reflections or diffraction) prevents clear analyses of potential~~
8 ~~further contributions.~~

9 For the laser operation we just slightly tilted the etalon vertically in order to avoid specular reflection. The
10 wavelength is changed by horizontally tuning the etalon that is mounted on a motorized rotation stage (OWIS).

11 For monitoring the emission spectrum an inexpensive computer-controlled miniature grating spectrograph is
12 used (Ocean Optics, HR 4000; $\Delta\lambda = 0.07$ nm). The performance of this spectrograph is highly satisfactory and
13 stable as determined from a comparison of the 308.955-nm emission that is reproducibly obtained for maximum
14 laser emission. Both the emissions around 308 nm and 353 nm are within the limited measurement range.

15 In Fig. 5-4 we show a typical spectrum obtained with the HR 4000 spectrograph. The etalon was rotated to
16 concentrate the pulse energy is concentrated almost exclusively in the low-wavelength spectral component. The
17 line shape is slightly asymmetrical with higher wavelengths indicated at the top than at the bottom. The etalon
18 angle was not fully optimized to show the small impurity peak at 308.4 nm that is located at twice the distance
19 between the strong line groups in Fig. 2 and is, thus, most likely corresponds to another, weaker line of XeCl.

20 ~~For the highest powers achieved this impurity grows, but stays in the range between~~Under optimum conditions
21 the impurity stays in the range between 1.0 and 1.5 %. Further suppression would require an etalon with a
22 slightly larger free spectral range.

23 The contribution of the longer-wavelength doublet (308.2 nm) for an optimum etalon angle is less than 0.5 %.
24 This value is in reasonable agreement with the 7 mJ of initial forward emission (Sect. 2.1), considering that just
25 one half of this weak broadband emission goes into the correct wavelength component (Fig. 2).

26 Given the specified 0.0507-nm resolution of the HR 4000 spectrograph the laser bandwidth is approximately
27 0.0503 nm. ~~This is larger than in good agreement with~~ the 0.0357 nm in the spectrum measured by Coherent in a
28 high grating order (Fig. 2). ~~Therefore, we expect an emission bandwidth of less than this value.~~

29 It is interesting to note that with an initially pronounced vertical tilt of the etalon we had achieved continuous
30 single-line tuning of the laser, however with changing output pulse energy as a function of the horizontal tilt
31 angle.

32 **Polarizer**

33 Linear polarization is mandatory for single-line stimulated Raman shifting (Kempfer et al., 1994) and for the
34 wavelength-separation strategy in our receivers (Sec. 3.2). Therefore, a thin-film polarizer was mounted in the
35 extended laser cavity, in the expanded section of the beam where the intensity is reduced. Despite the widened,
36 quadratic beam profile the substrate and the holder get rather warm after long operation of the laser at full power.
37 This is caused by the absorption losses due to a maximum transmittance of just 94 %. Nevertheless, the degree
38 of polarization of the laser output is as high as 99.4 %, in agreement with the expected 3.5 mJ (Sect. 2.1) of
39 forward emitted radiation with wrong polarization after the first passage through the laser medium.

1 Laseroptik meanwhile promised the capability of producing thin-film polarizers with more than 99 %
2 transmittance (as demonstrated for the polychromator). This would significantly reduce the thermal load and the
3 intracavity radiation losses.

4 *Alignment drifts*

5 A careful warm-up procedure was seen as mandatory because of the long resonator. Any small thermally
6 induced misalignment leads to a pronounced rotation of the laser beam inside and outside the cavity which can
7 lead to damage of components. Horizontal misalignment of the cavity starts to progress with growing repetition
8 rate that requires to rotate both the etalon and the end mirror horizontally. If the optical surfaces of the etalon
9 stay perfectly parallel the latter is difficult to understand and is tentatively ascribed to a combination of a slight
10 mutual distortion of the etalon plates and the cylindrical telescope. Vertical corrections are mostly negligible.

11 Warm-up has been performed in 50-Hz steps. For each step, etalon and end mirror are realigned for maximum
12 power after about five minutes of thermal equilibration. Very importantly, Maximum-maximum power
13 corresponds to optimum beam pointing and optimum spectral purity, which is highly welcome in view of
14 automatic control of the modified laser. At the end a highly stable operation of the laser is achieved over many
15 hours rarely requiring intervention.

16 For safety, six sand-blasted aluminium apertures were added as shown in Figs. 1 and 3, the first five of them
17 with a cross section of $43 \times 43 \text{ mm}^2$, the last one in the expanded beam (width = 200) \times (height = 120)-mm². As
18 mentioned, inside the laser cavity even weak reflections can lead to damage at maximum repetition rate. Outside
19 the laser head the apertures also help to control the beam pointing. At full power metal plates must be used to
20 localize the beam instead of paper sheets.

21 *Laser Pulse Energy*

22 In Fig. 6-5 the dependences of the pulse energy on repetition rate and load voltage, measured with the modified
23 system, is shown. For each measurement both end mirror and etalon were optimized.

24 The maximum pulse energy for a load voltage of 1.95 kV was 797 mJ without etalon and 765 mJ with the etalon
25 installed. This is much less than the 1.24 J at 1.95 kV and 300 Hz repetition rate achieved with the laser at the
26 factory. Of course, there are considerable intra-cavity losses. These losses are mostly caused by the polarizer and
27 the etalon, but perhaps also by deficiencies in imaging in the cylindrical telescope or by achieving less round
28 trips within the elevated-gain period due to the longer cavity. However, the overall losses are considerably
29 stronger than the optical losses, as we estimate from the moderate reduction in pulse energy when inserting the
30 etalon. We conclude that the most important drop in power is caused by the reduced number of round trips in the
31 extended cavity.

32 With growing repetition rate the energy first increases, but above 150 Hz it starts to drop considerably. This
33 behaviour is not similarly pronounced without the etalon as shown for comparison. It is, thus, ascribed to thermal
34 stress in the etalon. The optimum pulse energy at 350 Hz achieved for clean optics was 515 mJ, resulting in a
35 power of 180 W, one order of magnitude higher than in 355-nm Nd:YAG-based water-vapour Raman lidar
36 systems in the past. The power slowly decreases further during a long night-time measurement period, most
37 likely due to growing thermal issues. Under typical conditions we have operated the lidar in the range of 400 to
38 450 mJ, with aged gas even less. The pulse repetition rate was set to 300 Hz because of a time limitation in the
39 data-acquisition system for operation with 16000 bins.

40 The pulse energy at low repetition rate rises from 499 mJ at 1.55 kV to 777 mJ at 2.0 kV (lower panel of Fig 65).

Irupdlhu#&fkjhvwwoow

Irupdlhu#&kuliw@l#k#hww

Irupdlhu#&kuliw@l#k#hww

Irupdlhu#&kuliw@l#k#hww

2.3 Raman Shifter and Beam Expander

As routinely done in stratospheric ozone DIAL systems we first applied stimulated Raman shifting in high-pressure hydrogen for generating an “off” wavelength of 353.144 nm (Sec. 3.2) as a base for ozone corrections and a high-altitude temperature Rayleigh detection channel. We assumed that a conversion efficiency of a few per cent are sufficient for these purposes. In this way we could fulfil two goals, to minimize the loss of pulse energy in the fundamental wavelength for maximizing the detection sensitivity for water vapour, and to reduce the uncertainty in the pulse-energy level at 308 nm needed for calibration of the H₂O Raman detection channel.

One traditional problem with stimulated Raman shifting are losses due to the generation of high Stokes orders and due to optical breakdown, that can, according to our experience, efficiently be accomplished even with a long focal length of 1 m (Kempfer et al., 1994; Trickl et al., 2020b). Thus, we followed the design of the stratospheric ozone DIAL at Table Mountain (McDermid et al., 1991, and personal communication) and first selected an $f = 2.0$ m focussing lens. The length of the high-pressure cell is 3.6 m.

Indeed, the measurements at low repetition rates confirmed that just the first Stokes order was generated and the transmitted pump and Stokes energies summed up to 100 %. For 780 mJ emitted by the laser (without etalon) at a repetition rate of 10 s⁻¹ 19 % conversion into the first Stokes order was measured (Fig. 6). However, the 353-nm energy conversion efficiency at high repetition rates ~~was much lower did not exceed 3 % at a repetition rate of 350 Hz (Fig. 6), and just observable for slightly misaligning the cylindrical telescope in front of the laser (Fig. 1). With perfect collimation the first Stokes conversion disappeared for repetition rates of roughly 100 Hz and more. This required very critical astigmatic focussing influenced by a cylindrical beam expander in front of the laser (no longer used, therefore missing in Fig. 1). With a well-collimated laser beam no conversion was achieved at all at repetition rates beyond 100 Hz, even when we lowered the threshold energy with the finally used $f = 1.75$ -m lens (Fig. 1).~~

~~For increasing conversion efficiency, we replaced the focussing lens by an $f = 1.75$ m lens. This resulted in a significantly higher conversion efficiency at a repetition rate of 10 Hz. However, the conversion broke completely down after 0.5 min of operation when we increased the repetition rate to 100 Hz and more, which confirms our view of overloading the hydrogen gas in the foecal volume. The performance critically depends on the alignment of the components in the laser cavity and the cylindrical beam expander outside the laser. Therefore, the external beam expander was removed which resulted in a more stable performance at least up to moderate repetition rates. A new approach was introduced that is described below. The Raman shifter was then used just as a vacuum cell for the beam expander to avoid optical breakdown in air.~~

2.4 New Approach with a Frequency-Tripled Nd:YAG Laser

Instead of spending more time for Raman-shifting experiments, e.g., with longer focal lengths or a pair of crossed cylindrical lenses (Perrone and Picinno, 1997), we integrated in 2018 the injection-seeded Nd:YAG laser previously used in the water-vapour DIAL (Continuum, Powerlite 8020 Precision) into the system. This laser, modified for optimum beam quality for pumping a single-mode optical parametric oscillator, yields a reduced third-harmonic (355 nm) pulse energy of 160 mJ at a repetition rate of 20 Hz. This is sufficient for reasonable measurements (Sect. 6.2).

The use of this laser for providing the “off” wavelength has two advantages. Firstly, the full, stable power of the XeCl laser is available for the sounding of water-vapour, important for the H₂O calibration. Secondly, the

Irupdwlhu#ihijhvwhoow

1 Nd:YAG laser is run delayed with respect to the XeCl laser. In this way interference of the 355-nm Rayleigh
2 return in the H₂O Raman channel is completely excluded.
3 The Powerlite laser is meanwhile operated under control of an external computer, and synchronized with the
4 XeCl laser.

5 **2.5 Conclusions for the laser system**

6 Based on previously available laser specifications we had planned an average laser power of about 200 W,
7 ensuring an order-of-magnitude increase with respect to frequency-tripled Nd:YAG lasers most commonly used
8 in this field. Thus, the maximum single-line output of 180 W achieved in this project is acceptable. Also the high
9 degree of polarization fulfils the requirements for the new lidar.

10 Nevertheless, the significant loss of power with respect to the free-running laser is a major disappointment.
11 Solutions could come from injection seeding or shortening the laser cavity. We currently exclude injection
12 seeding since this would add significant costs and complexity. Shortening means a removal of the cylindrical
13 beam expander. This would enhance the intensity in both the etalon and the thin-film polarizer. However, as we
14 learnt from Laseroptik, both optics can be meanwhile manufactured almost without optical loss. In this way, the
15 thermal problems are minimized.

16 An important result is that for maximized output the beam pointing is extremely reproducible. Because of this
17 property we have meanwhile started to develop automatic power optimization by horizontal rotation of both the
18 etalon and the end mirror.

19 **3 Receiver design**

20 **3.1 General Design Considerations**

21 As also pointed out by Trickl et al. (2020b) the receiver design of the IFU lidar systems follows a number of
22 design principles:

- 23 (1) We use Newtonian telescopes for a less critical alignment.
- 24 (2) We separate the return in near-field and far-field channels because of the giant dynamical range of the
25 backscatter signal (see Sec. 4.3).
- 26 (3) No optical elements or detectors are placed close to the focal points in order to avoid a modulation of the
27 backscatter signal by the near-field scan of the focal point across inhomogeneously transmitting or detecting
28 surfaces. This prohibits the use of optical fibres because of their unknown input surface quality (apart from
29 coupling losses which mean throwing away a lot of the costly laser photons).
- 30 (4) Particularly inhomogeneous surfaces (such as those of the photomultiplier tubes (PMTs) used in our
31 system) are placed in or very close to image planes (exit pupils) where the image spots and the light bundle
32 as a whole stay stable in space. This also ensures that drifts in laser pointing have no influence on the
33 position of the spot of the returning radiation on the detectors even for very long beam paths, resulting in a
34 long-term stability as long as the no part of the light bundle is cut off by a holder or an aperture.
- 35 (5) The expensive interference filters are also placed in exit pupils to keep their diameter as small as possible.
36 The interference filters are placed in a collimated part of the radiation bundle to minimize angular spread. In
37 this way the near-field overlap is maximized.
- 38 (6) All lenses with focal lengths below 0.2 m are anti-reflection coated in order to avoid angle-dependent
39 transmittances.

1 3.2 Telescopes

2 Two separate Newtonian telescopes are used with focal length $f = 2$ m and diameter $d = 0.38$ m (Intercon
3 Spacotec, taken from our former eye-safe aerosol lidar (Carnuth and Trickl, 1994; Trickl, 2010), and with $f = 5.0$
4 m, $d = 1.50$ m (Astrooptik Philipp Keller), respectively. The large focal length of the far-field telescope
5 necessitated to install the receiver system in a separate tower on the terrace above the lidar (Fig. 86). The tower
6 (Sirch and Hägele&Böhm) is covered by a 4.2-m-diameter astronomical dome with a 1.50-m slit (Baader
7 Planetarium) which had proved to be an adequate solution under the arctic conditions on the high mountain. The
8 entire structure is designed for withstanding wind speeds up to more than 300 km h^{-1} . The costs for the dome
9 limit its size, and the slit width determines the width of the large telescope. Tower and dome were transported to
10 the site by a big Kamov double-rotor helicopter (HELISWISS), the large mirror with a small helicopter from
11 Heli Tirol. The mirror was lowered to the terrace, from where it was moved into the tower under assistance of
12 two provisional cranes.

13 Although the frame of the large telescope is prepared for heating this turned out to be unnecessary because of a
14 powerful heating system inside the tower. The tall frame carries both the secondary mirrors and the two
15 polychromators without contact to the measurement compartment that is stepped on by the operators. The tower
16 can be entered by two doors at the terrace level and upstairs. The upper door allows us to access the
17 measurement compartment directly or to use the emergency exit also after a major snowfall.

18 3.3 Polychromators and Wavelength Separation

19 The final design of the polychromators is shown in Fig. 79. The optical table (OPTA G.m.b.H.) is in reality
20 oriented vertically with the left-hand side representing the top. The entrance of the radiation arriving from the
21 telescope is horizontal (see Fig. 8), i.e., rotated with respect to the drawing plane, as one can see from the change
22 in polarization vector (dot for out-of-plane to double arrow for in-plane orientation). The radiation bundle is
23 spatially filtered with a rectangular aperture with four adjustable blades (custom-made by OWIS) placed in the
24 focal plane. Due to space limitations the aperture is oriented perpendicularly to the beam axis. A slight tilt angle
25 would be superior because of the longitudinal walk of the “focus”. This will be made possible in the future by
26 mounting additional inclined apertures in front of the PMTs. In this way, also the different diameters of the focal
27 points, caused by the different beam divergences of the two lasers, can be accounted for.

28 Several relay-imaging modules formed by confocally arranged $f = 150$ mm lenses (f_1) are seen (Sec. 3.1; see also
29 (Vogelmann and Trickl, 2008)). In the sections with parallel beams (with one exception) beam splitters and
30 interference filters are placed in or close to image planes of the primary mirror. Another confocal pair of f_1
31 lenses (not shown) is used to transfer the radiation from the focus of the large telescope to the first focal point in
32 the polychromator. The short-f lenses (f_2) image the principal mirror on to the photocathode of the
33 photomultiplier tubes (PMTs). The exact positions of the intermediate and final exit pupils can be nicely
34 identified with visible sky light after removing the interference filters.

35 ~~The design in Fig. 9 differs from that described in (Klanner et al., 2012) that was used until 2017. The~~
36 ~~modifications are related to the new laser concept (Sect. 2.3).~~

37 The specifications of the polychromators are listed in Table 2, including the lidar vacuum wavelengths and the
38 Raman shifts used. The Raman shifts in Table 2 sometimes differ from those in the lidar literature. The radiation
39 for the different wavelengths are separated by dichroic beam splitters and narrowband interference filters. This is
40 a highly demanding task considering the eight to ten orders of magnitude in signal between the Rayleigh and
41 Raman channels (Sec. 4.3). Figure 9-7 shows the principal polychromator design without the black walls

1 separating the detection compartments or surrounding the filters. In order to save costs, the optics of both
2 polychromators are equal for except for focal length f_2 that is chosen to achieve image diameters of the order of
3 5 mm for the different primary mirrors.

4 The optics (Table 3) were mostly purchased from Laseroptik G.m.b.H., with the exception of the narrow-band
5 interference filters and the steep-edge long-pass beam-splitters 5 and 6 (Materion Barr; beam splitter 6 is not
6 shown in Fig. 97). The width of the interference filter for water vapour (347 nm) was chosen to cover the entire
7 rather wide Q branch of H₂O in order to avoid a temperature influence on the backscatter profiles. A broad-band
8 interference filter (IFB; Semrock; $T = 85\text{-}90\%$) ~~just transmitting the Raman return and that at 353 nm (355 nm)~~
9 was ~~recently added for additional suppression of a potential residual influence of radiation outside the~~
10 ~~wavelength range of the Raman returns such as nin-order-to-eliminate~~ scattered light from illuminations inside
11 the laboratory, ~~and from the buildings of the ski area or R~~residual 308-nm contributions ~~are also removed~~.

12 ~~The design in Fig. 7 differs for the two long-wavelength channels from that described by Klanner et al. (2012),~~
13 ~~used until 2017. The old approach to separate the 347-nm and 353-nm returns was based on a pair of beam~~
14 ~~splitters with steep spectral edge (BS 6 in Table 3) similar to those used for separating the N₂ channel. The~~
15 ~~angular alignment for optimum H₂O signal was very critical, which is not helpful for a stable performance with~~
16 ~~stable calibration. The modifications in Fig. 7 remove the alignment-dependent signal loss in the H₂O channel.~~
17 ~~They benefit from the new laser concept (Sect. 2.3): The 355-nm pulses are temporally shifted with respect to~~
18 ~~those at 308 nm. In this way any residual 355-nm interference in the 347-nm channel is avoided.~~

19 Some of the components have been replaced by new ones with better performance over the years, i.e., polarizing
20 beam splitter 1 ($R > 99\%$ for 308 nm), and the interference filter in channel 2. The latter filter now suppresses
21 radiation at the pump wavelength to a level of about 2×10^{-4} . The low transmittance of the shorter-wavelength
22 interference filters is disappointing, but slightly exceeds that quoted. However, $T = 55$ to 65% for a $\Delta\lambda = 0.1\text{-nm}$
23 filter has been achieved at 386.7 nm by the same manufacturer in the past (Whiteman et al., 2010).

24 ~~Originally, a pair of 45° sharp edge beam splitters was also used to separate the H₂O channel from the 353 nm~~
25 ~~channel (Klanner et al., 2012). This worked extremely well: no 308 or 353 nm Rayleigh background was~~
26 ~~observed at 347 nm. As to 353 nm, the beam splitters reduce this spectral contribution by four decades, and the~~
27 ~~interference filter suppresses the “out of band” spectral contributions by more than six decades. However, the~~
28 ~~rise of the transmission function of these edge filters was not steep enough to minimize simultaneously signal~~
29 ~~losses at 347 nm and contributions at 353 nm. This was acceptable during the test phase when mostly no 353 nm~~
30 ~~emission was available at full repetition rate (see Sec. 2.2): The H₂O signal was maximized by rotating the beam~~
31 ~~splitters. It is obvious, that a slight angular misalignment could result in an undesirable change of the H₂O~~
32 ~~calibration. The new design shown in Fig. 9 no longer contains these beam splitters and leads to a more robust~~
33 ~~performance of the H₂O Raman channel.~~

34 3.4 Detectors and Discriminators

35 The detector choice is based on the experience from our stationary ozone lidar system. The final development
36 stage took place parallel to that for the ozone DIAL and is described in ~~more details~~ in (Trickl et al., 2020b).
37 Hamamatsu R7400U-03 tubes were chosen and integrated in an actively stabilized socket optimized for us in
38 1999 for our three-wavelength aerosol lidar by Romanski Sensors (RSV). The socket is now modified to deliver
39 optimized single-photon spikes without the ringing of the original PMTs that had previously enhanced the count
40 rate in our ozone DIAL up to about 5 km (Fig. 108). ~~The power connection cable is shielded, but the shield is~~
41 ~~grounded just on one side. The RSV socket generates a clean reference voltage (5 V), produced from the 15 V~~

1 supply voltage. The 5-V reference, corresponding to a PMT voltage of 1000 V, is then returned to the power
2 supply where it is divided to the adjustable final control voltage level (0 to 5 V) sent back to the detector. It is
3 important to note that this loop was necessary to clean the lidar signals to a level below 10^{-5} of the peak signal.

4 Signal-induced nonlinearities can be avoided for normal operating voltages around 800 V if one limits the
5 analogue signal to roughly 100 mV or less (Trickl et al., 2020b). This level is high in comparison with traditional
6 PMTs. Nonlinearity in the photon-counting signal revealed by a comparison with a simultaneous ozone
7 measurement at Hohenpeißenberg for analogue signals of 400 mVIn one measurement at 308 nm requiring to
8 enhance the signal to more than 400 mV we detected deviations of the photon-counting signal from the
9 corresponding signals obtained at the Hohenpeißenberg station (43 km to the north) during the same night
10 suggesting a signal-induced contribution.

11 The output of a PMT is fed into an impedance-matched junction containing the discriminator (RSV). The output
12 for the analogue channel is slow, with single-photon pulses widened by a factor of two. The second branch is the
13 fast discriminator that emits -0.4 -V constant amplitude pulses with a full width at half maximum of 0.6 to 1.5 ns,
14 depending on the photon pulse height. The discriminator level that can be chosen from -2 mV to lower voltages.
15 This is important for the six-dynode PMT and its rather small pulses. The pulse-height distribution for 800 V
16 peaks at about 10 mV (Fig. 449). We have applied discriminator levels between -4 and -5 mV.

17 An important issue for achieving a high sensitivity is a low level of dark counts photons, which normally
18 requires to cool the PMT (0.03 counts s^{-1} ; Trickl and Wanner, 1981). With the PMTs used here and
19 discriminator levels of -4 mV no dark count was registered in 50-ns bins within one hour (1×10^6 laser shots)
20 without cooling. The average external background for atmospheric measurements is clearly less than 1 count for
21 voltages up to the maximum of 1000 V, except for the H₂O channel (see Sect. 6). In the H₂O Raman channel a
22 supply high voltage of up to the maximum 1000 V was used for maximizing the analogue signal that was of the
23 order of just a few mV at a distance of 1 km (3.7 km a.s.l.), because of the considerable dryness in the free
24 troposphere. For the measurements typically 900 V were chosen.

25 3.5 Transient Digitizers

26 Following the other lidar systems developed at IFU since 1995 we purchased two 12-bit, 20 Hz transient
27 digitizer systems from Licel, each with six channels. Licel designed for this project and the ozone DIAL new,
28 ground-free input amplifiers. This latest version has led an unprecedented performance in the ozone DIAL with a
29 relative noise level of about $\pm 1 \times 10^{-6}$ of the full voltage range after minor smoothing, yielding also highly
30 sensitive aerosol measurements at 313 nm despite the short wavelength (Trickl et al., 2020b).

31 An exponentially decaying contribution of roughly 10^{-5} of the peak signal is present that scales as the signal
32 pulse area, i.e., grows with the wavelength. This contribution differs in slope from that in the ozone DIAL,
33 presumably because of additional electronic components used. The artefact is more likely to be produced by
34 combining the different units than by the PMT itself. After introducing the discriminator for the photon-counting
35 channel and the counter the exponential wing increased and a slight undershoot occurred in addition. The
36 interference could be strongly reduced by adding an optocoupler to the trigger input of the counting system
37 (Sect. 3.6). Some more sophisticated impedance matching is necessary for achieving an ultimate performance.
38 Examples for the performance so far achieved are shown in Sect. 6.

39 Another limitation has resulted from the high data transfer produced by the chosen 16000 bins (120 km): The
40 repetition rate of the laser had to be limited to 300 Hz in order to allow for a reliable data storage.

1 3.6 Photon counting

2 Single-photon counting is mandatory in a lidar system with stratospheric capability. In order to benefit from the
3 temporal resolution of the PMTs we purchased MCS6 and one MCS6A five-channel photon counting systems
4 from Fast Comtec. Just two of them were used at the end since the analogue signal range for the near-field
5 receiver was found to be good enough to do without photon counting.

6 The signals are scanned for falling edges at intervals of 100 ps which means a maximum count rate of about 5
7 GHz for equidistant picosecond pulses. ~~Three systems seemed to be necessary for our 12 detection channels
8 since one input channel of each MCS6A is used as a trigger input. However, testing the near field receiver
9 showed that photon counting is not required there.~~

10 A bottle neck of this counting system is the sequential data transfer to the computer that limits the signal to
11 $1.8 \times 10^7 \text{ s}^{-1}$ ~~per 100 ns~~. The multi-channel scaler was, therefore, triggered with a delay of 10 to 20 μs with
12 respect to the laser pulse which resulted in a fully linear performance for H_2O . However, if an earlier beginning
13 of the individual measurement is desired on-board averaging becomes necessary that is not implemented in this
14 model. Another limiting issue has ~~ed~~ been the control program of the counting ~~system-system: An automatic start
15 from outside UFS is not reliable and a "mouse click" on the "start" symbol is needed on the remote
16 computer, that sometimes blocked the start of the data acquisition. A new update of the program has led to more
17 reliability, but has not been tested long enough for a conclusion.~~

18 3.7 System Control

19 The electronic components of the two DIAL systems (Ingenieurbüro W. Funk) are ground-free. The trigger pulse
20 is derived from a photodiode and subsequently distributed into numerous output channels via optocouplers. The
21 supply voltages are transferred to the different devices in shielded cables. The shields of the cable leading to the
22 PMTs are open on the side of the detectors. The supply voltage can be set by the lidar PC via an I²C bus. Electro-
23 magnetic interference in the lidar signals from outside (e.g., the laser) has been kept at a negligible level by using
24 doubly shielded cables (Suhner, G03332; the outer shield is left open on one side) and ground-free circuits.

25 The data acquisition of the lidar system is controlled from a central Linux computer via a perl program and
26 ethernet. The Licel transient digitizers are fully read every 10 seconds. At a repetition rate of 300 Hz this allows
27 for an integration without overflow due to 24-bit depth for each unit. This data stream is subsequently integrated
28 for each channel by the controlling program until the end of the measurement after one million laser shots
29 corresponding to an integration time of roughly one hour. The measurement data is finally stored in an ASCII
30 file including meta information in the file header.

31 The same perl program is designed to control also the photon counting devices via ethernet communication with
32 the Windows based FASTComTec software. ~~As mentioned, t~~his communication does not yet work reliably for
33 control from outside UFS.

34 Meanwhile, the excimer laser can be operated via Ethernet, as well as the rotation of the etalon, the spectrometer
35 HR400 and a new motorized ~~resonator~~-end mirror of the XeCl laser. The laser power supply and cooling water
36 pump are controlled by Wago-SPS units (programmed in CodeSys) via a Java web interface. The beam steering
37 mirror is motorized and remotely controlled with a custom made software from ASA. The slit of the lidar dome,
38 the covers of the telescopes, the laser output mirror and the power supply of the lidar receiver are controlled with
39 a Wago-SPS system via a Java Web interface.

40

4 Data Processing

4.1 Water Vapour

A great advantage of a Raman lidar is that uncalibrated H₂O ~~concentrations-densities~~ are obtained in a ~~direct~~ robust way by multiplying the backscatter signal for the full ro-vibrational Q branch by the square of distance r (range correction). Thus, small perturbations of the signal do not matter as severely as in the DIAL algorithm that implies derivative calculations. However, in our system the choice of a particularly powerful UV laser implicated a short operating wavelength of 308 nm. Thus, for obtaining number densities an ozone correction must be made that is based on the DIAL solution for the wavelengths 307.955 nm and 353.11 nm (or recently 354.22 nm).

For simplicity we have so far preferred to calculate just water-vapour volume mixing ratios, which also makes a range correction superfluous. The uncalibrated mixing ratios are calculated by dividing the H₂O backscatter signal by the vibrational nitrogen Raman backscatter signal. Here, the influence of ozone exactly cancels on the upward path because the transmitted wavelength is the same for both Raman channels. On the downward path a small residual absorption in the stratospheric ozone exists at 331.75 nm that grows to almost 2 % at 20 km and has been neglected given the current level of accuracy at this altitude. The photon counting data are collected at 51.2 ns per bin instead of the 50 ns in the transient digitizers and are interpolated to match the time scale of the analogue data. In order to avoid excessive data array sizes, we double the bin size to 100 ns during the subsequent calculations, averaging pairs of neighbouring signals,

In the useful range for H₂O up to roughly 20 km the relative noise of the nitrogen Raman signal is negligible and no smoothing is applied. Smoothing is just applied to the Raman signal ratios that are determined separately for the analogue and the photon-counting data. The smoothing approach is based on a numerical low-pass filtering approach with Blackman window described and characterized in the parallel paper by Trickl et al. (2020b). This numerical filtering approach is free of ringing. The filtering interval is dynamically increased. As shown in Sec. 6 a purely quadratic dependence

$$L = 1.2 \times 10^{-4} i^2$$

as a function of 15-m bin i (minimum interval size: 2 bins, $i \leq 300$) (or slightly modified for noisier data) is adequate. In one case (5 February 2019) a third-order polynomial was used for L to achieve a better vertical resolution in the lowermost stratosphere in the presence of a steep concentration feature. In a Raman lidar this dependence does not require much modification from measurement to measurement, whereas in a DIAL the strongly changing water-vapour concentration results in considerable change in absorption and, thus, of the smoothing requirements. The definition of vertical resolution so far used by us is given by the range interval corresponding to the 25 % to 75 % rise of the response of the smoothing filter to a Heaviside step (VDI, 1999). For the Blackman filter the VDI vertical resolution is 19.3 % of the size of the smoothing interval. Leblanc et al. (2016) recommend to define the vertical resolution as the full width at half maximum of a delta response which is 34.7 % of the filtering interval for the Blackman filter. Equation 1 yields a VDI vertical resolution of 155 m at 10 km, 348 m at 15 km and 619 m at 20 km, and a delta-response vertical resolution of 277 m at 10 km, 624 m at 15 km and 1109 m at 20 km.

The role of aerosols is limited to extinction and, in the case of biogenic particles (Immler et al., 2005; Reichardt et al., 2017), to fluorescence in a Raman lidar. The presence of aerosols is best judged from the 355-nm channel.

1 The influence of extinction is very low when calculating the H₂O mixing ratio from the ratio of the H₂O and N₂
 2 profiles. An estimate of the extinction coefficients at the two wavelengths can be obtained from the 355-nm data.
 3 The system testing was limited to clear nights. Thus, aerosol effects could be neglected.

4 4.2 Temperature

5 The retrieval of temperature from lidar data is a highly demanding task. For instance, an uncertainty of 1 K
 6 means a relative uncertainty of 0.33 % at a temperature of 300 K. Thus, a very high quality of the backscatter
 7 signals is a prerequisite for reasonable results. For our system the two conventional methods have been selected,
 8 evaluating the temperature dependences of the rotational Raman spectra received just below 308 nm (Arshinov
 9 et al., 1983) and the direct retrieval of temperature from backscatter profiles (Hauchecorne and Chanin, 1980).

10 The retrieval of temperature profiles from rotational Raman backscattering has not yet been optimized and is,
 11 thus, not described here. The main problem has been that the first generation of 307.390 nm interference filters
 12 obtained from Materion Barr did not sufficiently reject the 307.955-nm contribution. In principle, this
 13 contribution is a reasonable reference in the absence of aerosol because it is independent of temperature. Thus,
 14 several successful temperature retrievals could be achieved for the near-field receiver (Höveler, 2015).

15 The evaluation of temperature profiles directly from backscatter profiles has been tested for the Rayleigh
 16 channels at 308 nm, 353 nm, 355 nm as well as the nitrogen Raman channel (332 nm). Due to the signal losses
 17 caused by ozone the range of the N₂ channel is limited. We finally decided to invert the backscatter signal for
 18 355 nm (Sec. 2.3). The analogue and photon counting backscatter profiles are merged into a single profile,
 19 switching at about 28 km. The resulting profile is, again, smoothed with the Blackman filter mentioned above.
 20 Similar to water vapour the filtering interval Δ is enhanced as (approximately)

$$21 \quad L = 2 \times 10^{-5} i^2$$

22 as a function of 15-m bin i .

23 We follow the strategy of calculating the temperature described by Shibata et al. (1986). In a first step the
 24 density is calculated and subsequently the temperature. However, instead of the simplified density algorithm we
 25 use a fully quantitative Klett-type approach with downward integration from the far end (Klett, 1981; 1985). The
 26 result is calibrated to the number density n and not to the backscatter coefficient:

$$27 \quad n(r) = \frac{n(r_{ref}) r_{ref}^2 S(r_{ref})}{r^2 S(r) + 2n(r_{ref}) \sigma_R \left[1 + \int_r^{r_{ref}} r'^2 S(r') dr' \right]}, \quad (1)$$

28 $S(r)$ being the ozone-corrected backscatter signal, r_{ref} the reference distance and σ_R the Rayleigh extinction
 29 coefficient. We take as a first approximation a reference value calculated from NCEP (National Centers for
 30 Environmental Prediction, <http://www.ncep.noaa.gov/>) data. The NCEP values are available up to a geopotential
 31 altitude of 50 km. Beyond this, initial guesses from the U.S. Standard Atmosphere (1976) are taken, after
 32 converting the geopotential altitudes into real ones ([as in the case of the NCEP data](#)). The results of the inversion
 33 with Eq. 1 are then compared with radiosonde or NCEP values in a low-noise range of the backscatter profile at
 34 moderate altitudes. If the agreement in this reference range is not sufficient, $n(r_{ref})$ is modified, and the procedure
 35 is repeated until agreement is reached. This approach is highly robust, a change in reference value corresponding
 36 to an approximate parallel shift of the curves. For the selection of r_{ref} , it is advisable to select a position for which

1 the signal $S(r_{ref})$ is closest to the average of adjacent data points. In this way, the subsequent correction
 2 necessitated by the local data noise are the lowest.
 3 The temperature is subsequently calculated from the density by applying

$$4 \quad T(z) = T(z_0) \frac{n(z_0)}{n(z)} + \frac{m_{air}}{k n(z)} \int_z^{z_0} n(z') g(z') dz' , \quad (2)$$

5 with z being the altitude above sea level, $m_{air} = 28.9644$ u (U.S. Standard Atmosphere (1976); 1 u =
 6 $1.6605390 \times 10^{-27}$ kg) the mass of an “average air molecule”, and g the gravitational acceleration (Mohr et al.,
 7 2014),

$$8 \quad g(z) = g_0 \left(\frac{r_E}{r_E + z} \right)^2 ,$$

9 with $g_0 = 9.80665$ m s⁻¹ and the earth radius $r_E = 6356766$ m.

10 Equation 2 immediately shows that selecting z_0 at the upper end of the data-evaluation range means a strong
 11 decrease with the growing density on the way downward. As a consequence, the second term in Eq. 2 clearly
 12 dominates the temperature about 15 km downward from z_0 . Here, the the number density retrieved in the first
 13 step determines the temperature. Any density error critically enters the computation of the temperature. Thus, the
 14 range of the temperature retrieval is shorter than that of the density retrieval.

15 4.3 Uncertainties

16 Uncertainties u of both water vapour and temperature have been approximated by the expression

$$17 \quad u = \sqrt{u_0^2 + \left(u_1 \frac{r^2}{r_{ref}^2} \right)^2 + (u_2 S(r))^2} , \quad (3)$$

18 with coefficients u_0 , u_1 , and u_2 that are adjusted by comparison with reference measurements as shown in the
 19 examples in Sect. 6. The second term in Eq. 3, quadratic in r , reflects the quadratic rise of the noise of the
 20 unsmoothed quantities. The reference distance r_{ref} is chosen at the upper end of the data evaluation range. By the
 21 approach with Eq. 3 considerable computation efforts have been avoided.

22 4.4 Simulation of the system performance

23 Before finalizing the lidar design a number of simulations of the system performance were made. Figure [12-10](#)
 24 shows the results for 200 W of laser power at 308 nm, a range bin of 200 m, 10 % detection efficiency and a
 25 measurement time of 1 h. The atmospheric data were taken from the mid-latitude summer model of the
 26 LOWTRAN simulation program (Kneizys et al., 1988).

27 It is obvious that the Raman backscatter signal for stratospheric water vapour is roughly eight orders of
 28 magnitude smaller than the Rayleigh backscatter signal for 308 nm. This imposes extreme boundary conditions
 29 for the optical system (Sec. 3.3). The effect of the signal loss at 308 nm due to the absorption by ozone is not
 30 very severe up to 20 km. In comparison with the most commonly used primary wavelength of 355 nm this loss is
 31 roughly compensated by the fourth-order frequency dependence of the Raman backscatter coefficient.

32 [As demonstrated by the atmospheric measurements the polychromators fully meet the requirements.](#)

33 5 Calibration of the water-vapour profiles

1 The calibration of the Raman lidar by the water-vapour DIAL operated in the same laboratory is a unique chance
2 to overcome the restrictions imposed by the sometimes extreme variability of water vapour (Vogelmann et al.,
3 2011; 2015). This variability is caused by a rapid sequence of atmospheric layers of strongly different origin.
4 The humidity varies from very high (origin in the boundary layer) to extremely low (origin in the stratosphere).
5 Our routine measurements since 2007 have revealed that on 84 % of our ozone measurement days stratospheric
6 influence could be identified in the free troposphere (Trickl et al. 2020a). This leads to a particularly strong
7 modulation of the humidity profile.

8 In Fig. 13-11 we show the first example of a comparison between the two lidar systems on 25 April 2013. The
9 measurements took place under highly complex conditions in the presence of three dry layers, two of them
10 clearly related to stratospheric air as follows from the almost negligible humidity. 315-h backward trajectories
11 with the HYSPLIT model (<http://ready.arl.noaa.gov/HYSPLIT.php>; Draxler and Hess, 1998; Stein et al., 2015),
12 run here with re-analysis meteorological data, show a 5- to 7-day descent from altitudes above 9 km over
13 western Canada and more than 10 km above the Aleutian Islands for the layers at 4.2 km and 6.7 km,
14 respectively.

15 This was the only case in our entire test phase in which a slight 308-nm background was superimposed on the
16 signal. This background could be reliably removed by subtracting a very simple exponential curve. After
17 calibration of the data from the Raman lidar with those from the DIAL above 5.5 km reasonable agreement was
18 found in a major fraction of the free troposphere. However, due to using the same electronics in that early phase
19 the measurements were not made simultaneously. Thus, a few differences are visible and ascribed to to
20 sometimes extreme spatial and temporal variability of water vapour (Vogelmann et al., 2011).

21 The strong variability becomes even more obvious from comparisons with the Innsbruck (32 km to the south-
22 east; shown) and Munich radiosonde (100 km to the north; not shown) ascents that differ strongly and do not
23 show similarly dry layers despite similar courses of the trajectories calculated for these sites in comparison with
24 those for the lidar station. This example demonstrates that simultaneous calibration of the Raman lidar with the
25 quality-assured DIAL (e.g., Trickl et al., 2016) is mandatory. Unfortunately, comparisons have no longer been
26 possible after 2014 due to a permanent laser damage of the DIAL. The development of a new Ti:sapphire laser
27 system with high repetition rate is under way and emission was already demonstrated.

28 The stability of the calibration can be monitored by using the signals of the 308-nm, 332-nm and 355-nm
29 channels outside ranges affected by aerosol.

30 During the rest of the test period in part described in the following the system was calibrated by comparison with
31 sonde humidity profiles from Munich, Innsbruck and Hohenpeißenberg, selecting sections of the sonde profiles
32 looking most reasonable. Geopotential altitudes are converted into true altitudes. During one night in February
33 2019 very successful comparisons with a CFH sensor (launched in the valley) were made.

34 6 Measurements in the Atmosphere

35 After the completion of the lidar systems testing started in autumn 2012. The measurements demonstrated the
36 perfect suppression of interference from the other channels in the water-vapour channel by spectral filtering and
37 shielding. This achievement implies, according to the simulations in Sec. 4.3, a suppression of more than nine
38 decades of 308-nm background.

39 In early 2015, the near-field receiver was completed and performed well. Even rotational Raman retrievals with
40 a temperature noise level of 1 K were achieved (Höveler, 2015). In addition, single-photon counting successfully
41 entered operation for the far-field receiver, but was given up for the small telescope because of the excellent

1 analogue performance. In the following, we show results just for the far-field receiver since a good system
2 performance at high altitudes has been the main goal of this project. The examples were chosen to show the
3 performance under different conditions such as different levels of background noise and different situations of
4 calibration.

5 6.1 Water Vapour Measurements up to 20 km

6 1 July 2015

7 The first measurement demonstrating a detection range up to 20 km was achieved on 1 July 2015 (Fig. 12). The
8 polychromator was, still, operated under testing conditions, i.e., just provisionally optically tightened against
9 light from the instrument panels inside the detection compartment to facilitate alignment studies. However, it
10 turned out that the only significant radiation leak was the wide entrance slit of the polychromator (about 40 mm
11 × 40 mm²). The strong background of 155 photon counts per hour in 15-m bins is ascribed to scattered radiation
12 from the almost full moon. Despite the resulting noise of ±25 counts the signal, arithmetically averaged over 52
13 bins, it stays positive to distances up to 19.7 km (22.4 km a.s.l.).

14 Figure 14 shows the water vapour Raman backscatter signals for this measurement. The signal was accumulated
15 over 1 h with a laser pulse energy of just 295 mJ (300 Hz) due to a dirty cell window. The analogue signal was
16 corrected just with a very small simple exponential correction $(740 \text{ counts}) \cdot \exp(-8.5 \times 10^{-5} \cdot i)$, i being the bin
17 number, leaving a slight residual signal undershoot is seen for distances around 12 km that is ascribed to the
18 parallel use of analogue detection and photon counting (Sec. 3.4). The peak analogue signal is about 3 mV, but is
19 rescaled here to match the counting signal. The photon-counting background is 155 counts h⁻¹ (15 m)⁻¹ and most
20 likely strongly influenced by the background from the almost full moon. The noise is much lower, about ±25
21 counts (standard deviation: 12.7 counts), and corresponds to an analogue voltage of just about ±15 nV.
22 Smoothing with a gliding 51-point arithmetic average (red curve in Fig. 14), corresponding to a VDI vertical
23 resolution of 375 m, yields non-negative H₂O signals up to r = 19.7 km (22.4 km).

24 Water vapour mixing ratios were calculated just by using the analogue data for nitrogen (corrected for a very
25 small exponential wing) because of missing data in the corresponding counting channel during this measurement
26 (Fig. 15). The calibration of the mixing ratio was very difficult since there was macroscopic mutual
27 disagreement of the lidar and all three Vaisala RS 92 radiosonde profiles inspected (Klanner et al., 2017, Fig. 3).
28 A few points below 7 km where the sonde data agree were chosen as reference. The Hohenpeißenberg mixing
29 ratio (early morning) agrees best with the lidar results in the tropopause region and is, therefore, displayed here.

30 The example of 1 July 2015 is special in our test phase; since there was very low water vapour around
31 15.7 km (about 2 ppm). The drop is verified by the Vaisala RS 92 sonde ascent at Hohenpeißenberg in the early
32 morning profile. Although the sonde data becoming highly uncertain at higher altitudes we see principal
33 agreement with the lidar. HYSPLIT trajectory calculations indicated advection of tropical air from the Caribbean
34 Sea above the tropopause, slightly downward shifted most likely because of a wrong model orography at the
35 northern rim of the Alps. In the tropics freeze drying in cirrus clouds has been suggested to lead to dehydration
36 and, thus, low humidity (see Sect. 1). Such an inhomogeneity is a strong motivation for lidar work that features a
37 potential for a good time resolution. Water vapour is an excellent tracer for troposphere-to-stratosphere transport
38 (TST) and there is some hope that we can study some cases of TST in the future.

39 Measurements since 2018

Trupdwlnh#*fkjhwwhoow

1 The measurements since 2018 were carried out with full optical insulation of the channels including the cover of
2 the polychromators, with narrow entrance slit and with measurements at 355 nm with the separate Powerlite
3 laser. In 2018 and until 6 February 2019, a total of 14 1-h measurements and several shorter tests were carried
4 out during nights completely without clouds. The minimum H₂O mixing ratios were 4 to 6 ppm, i.e., in the range
5 one would expect for the stratosphere from the literature cited in the introduction.

6 The finally chosen size of the horizontal entrance slit was roughly 4 mm × 8 mm, slightly larger than the
7 minimum that is determined by the product of the large beam divergence of the enlarged laser beam and the
8 focal length of 5 m (receiver). The background signal in 1 h ~~and~~ was mostly zero in all 7.5-nm bins (rarely 1
9 count) except for H₂O. Here, typically 3 to 5 counts were registered. In one case a narrower slit was used
10 (roughly 2 mm × 8 mm). This led to 1 to 2 background counts, but also to an indication of a lower backscatter
11 signal. This would be in agreement with the large beam diameter in the focal plane of roughly 2.5 mm as
12 expected from the laser beam divergence and the receiver focal length of 5 m.

13 The reason for the background counts in the water-vapour channel could not be fully clarified. Upper-
14 atmosphere air-glow spectra (Broadfoot et al., 1968; Johnston et al., 1993) show several features in the
15 wavelength range of the in the lidar return for $\lambda \geq 332$ nm. However, some spectral overlap also exists with the
16 components at 332 nm, 353 nm and ~~353-355 nm~~ where the background is very low. No clarification has been
17 possible.

18 **19 July 2018**

19 During the early hours of 19 July 2018, two subsequent measurements were made that could be compared. The
20 average laser pulse energy was just 380 mJ (300 Hz). The background count rate was 5-8 counts h⁻¹ bin⁻¹ for a
21 slightly larger entrance slit.

22 The mixing ratios obtained are shown in Fig. [4614](#). The calibration of the first measurement was estimated from
23 the Munich sonde data for the launch at 1:00 CET. The profile for the second measurement looks completely
24 different which, again, demonstrates the strong atmospheric variability of water vapour. Here, the calibration of
25 the lidar mixing ratios was based on the Innsbruck sonde (nominal daily launch: 4:00 CET). We assume that the
26 horizontal homogeneity is much better in the the tropopause region, where we, thus, centred the calibration.
27 However, the agreement is also reasonable around 6.5 km (5 to 10 %).

28 The two profiles for the lidar agree quite well up to about 18 km (Fig. [4715](#)), despite the elevated signal
29 background. The second measurement was noisier which is reflected by the larger error bars.

30 It is interesting to note that the sonde data are substantially lower than the mixing ratios from the lidar, which is
31 also the case in the following examples-do not look as reliable in the lower stratosphere as in the July 2015 case.

32 We speculate that this is due to a change in sonde type from RS 92 to RS 41 by the German Weather Service.

33 We have found that the RS 92 data highly realistic in our tropospheric studies in comparison with our DIAL
34 (Trickl et al., 2014-2016). For 2018, the data for the -new sonde type exhibited a positive bias of 2-3 % relative
35 humidity (RH) in intrusion layers.

36 **5 February 2019: system validation**

37 On 5 and ~~5-6~~ February 2019 several balloons with cryogenic frostpoint hygrometers (CFH; Vömel et al., 2007;
38 2016), standard Vaisala RS-~~41-41~~-SGP radiosondes (Vaisala et al., 2019), ECC ozone sondes (Smit et al., 2007)
39 and COBALD backscatter sondes (Brabec, 2011) were launched in the valley at IMK-IFU (9 km to the north-
40 east of UFS) by a team of the Forschungszentrum Jülich. The data were transmitted to a ground station installed

1 for this campaign at the Zugspitze summit. The combined balloon payload is well tested and regularly also used
2 by the GCOS Reference Upper Air Network (GRUAN) (e.g., Dirksen et al., 2014).

3 The CFH has an uncertainty of about 2-3 % in the troposphere and less than 10 % in the lower stratosphere.
4 Thus, the CFH is especially suitable for measuring water vapour under the dry conditions at the tropopause and
5 in the stratosphere up to altitudes of 28 km.

6 The first night of the campaign was clearer and these results are presented in the following. The conditions for
7 the comparison were excellent: the sondes rose almost vertically up to 8.5 km and then slowly drifted to the
8 south-east (Innsbruck). The balloons stayed within 20 km distance up to the tropopause (12.8 km a.s.l.) and
9 remained within 30 km from IMK-IFU up to 20 km a.s.l.

10 The launch times of the balloons were 18:03 CET (ascent to 16.147 km), 19:03 CET (29.475 km), and 23:00
11 CET (29.469 km). The profiles of the CFH H₂O mixing ratio during that period mutually agreed to within 0.5
12 ppm between 13.0 km and 17.5 km and slightly more up to 26 km. Just two of the three lidar measurements at
13 UFS cover the full standard measurement time of one hour and are presented here.

14 The H₂O Raman backscatter profile for the measurement before midnight is shown in Fig. 18.16. Due to a narrow
15 slit the H₂O raw data exhibit a background of just 2.33 counts (subtracted here) with a standard deviation of 1.55
16 counts. Two curves with gliding arithmetic means over ± 25 and ± 75 bins are included that suggest a useful range
17 up to $r = 17$ km ($h = 19.7$ km a.s.l.). The remarkably low sensitivity limit for the averaged curve corresponds to
18 roughly 0.1 nV of analogue voltage. The dynamic range within the dry free troposphere and the lower
19 stratosphere covers astonishing seven decades.

20 The nitrogen Raman backscatter signal is considerably larger. Thus, the onset saturation effects can be seen in
21 the photon-counting data below $r = 4$ km. Here, the analogue data are, still, valid for at least two more downward
22 kilometres. The analogue signal starts to deviate from the photon-counting signal due to an exponential decay in
23 the signal processing mentioned in Sect. 3.5. We do not correct this effect because the photon-counting method
24 is used at high altitudes.

25 Figures 19-17 and 20-18 show the water vapour mixing ratios obtained for two measurement periods on 5
26 February with 1-h lidar measurements together with those from the almost simultaneous CFH ascents. In
27 addition, the values for the Munich radiosonde (6 Feb, launched at 1:00 CET) are included for comparison. The
28 grey curve corresponds to the VDI vertical resolution used for the numerical filtering that is about 0.2 km at 14
29 km and 0.47 km at 20 km. Due to the moderate smoothing around 13 km the downward humidity step at 12.8 km
30 is just slightly widened with respect to the CFH sensor. We reduced the vertical resolution of the first
31 measurement around this step by introducing a third-order dependence (polynomial) of the smoothing interval
32 (Eq. 1), but could not improve the steepness of this step. We conclude that the width of the step in the lidar result
33 is primarily determined by the long data acquisition over 1 h.

34 The lidar was calibrated in the upper troposphere above 7.7 km yielding an almost perfect agreement with the
35 CFH measurements in this range. Between 7.7 km and 5.7 km it is, still, satisfactory with deviation of 5 to 10 %.
36 Below this altitude the agreement for the first profile was also acceptable, the lidar value lying in the middle of
37 the CFH mixing ratios for ascent and descent (the latter not shown for clearness). This was quite different for the
38 second profile recorded before midnight when the atmosphere was obviously highly inhomogeneous in space,
39 even on a horizontal scale of 10 km given by the almost vertical rise of the balloon. The presence of several very
40 thin dry layers, also over Munich, indicate a pronounced filamentation.

41 Below this zone the agreement is good for both measurements. This indicates a good cancellation of the overlap
42 functions of the nitrogen and water-vapour channels, similar to DIAL systems.

1 6.2 Temperature Measurements

2 *Rotational Method*

3 A few measurements based on the rotational temperature method were evaluated for the near-field receiver
4 (Höveler, 2015). The Cabannes influence was corrected for. A good performance with a temperature noise of
5 less than 1 K in a range up to 8 km in the free troposphere was achieved. With recently purchased new narrow-
6 band interference filters (Materion Barr rejection of Cabannes radiation to 2×10^{-4}) and a better polarizing beam
7 splitter (Laseroptik, $T > 99\%$) we expect a much better rejection of the Cabannes radiation.

8 *Rayleigh Method*

9 Temperature profiles based on the Rayleigh approach have been made for the wavelengths 308 nm, 332 nm, 353
10 nm and, finally, 355 nm. For 308 nm and 332 nm the signals must be corrected for the absorption of the radiation
11 in ozone. The range for 332 nm ends far below the mesosphere and is, therefore, no longer considered. For 308
12 nm a temperature retrieval up to 55 km was achieved. However, the backscatter signal was attenuated with a
13 neutral-density filter by a factor of one thousand in order to avoid detector overload. This means that, without
14 attenuation, a high-speed chopper must be added to cut off the signal returning from the first ten kilometres.
15 Then, the performance could be excellent. The 353-nm channel was successfully tested at low repetition rates
16 (yielding reasonable temperatures up to 52 km), but was given up because of the loss of Raman conversion at
17 full power.

18 Here, we present the first demonstration of a measurement with the separate frequency-tripled Nd:YAG laser
19 (Sect. 2.4) up to the mesosphere on 16 November 2018. This example yields the best example of the technical
20 performance of the UFS lidar: Figure 24-19 shows the backscatter signals for a 1-h measurement up to as high as
21 120 km. The smoothed combined signal (analogue at low altitudes, photon counting at high altitudes; cyan
22 curve) exhibits low to moderate noise up to 95 km (VDI vertical resolution: black curve). The average photon
23 counting background is considerably less than 1 count. This results in an overall dynamic range of 8 decades,
24 together with simulations. The analogue signal exhibits a considerable distortion at high altitudes which we
25 ascribe of the known (Trickl, 2010) magnetic interference of the Nd:YAG laser. Again, a correction is not
26 necessary because the photon-counting data are used at high altitudes.

27 For comparison, we give simulated backscatter profiles calculated for from the U.S. Standard Atmosphere and a
28 combination of the 1:00 CET Munich radiosonde and the 13:00 CET NCEP data for our station downloaded
29 from the NDACC web site. The curve for the standard atmosphere (green) is climatological and slightly deviates
30 from the lidar results at high altitudes. It just guides the eye. No deviation of the lidar backscatter profile with
31 respect to the sonde and NCEP data is seen up to end of these data at 53 km (blue curve). The analogue signal
32 exhibits a considerable distortion at high altitudes which we ascribe of the known (Trickl, 2010) magnetic
33 interference of the Nd:YAG laser. Again, a correction is not necessary because the photon-counting data are
34 used at high altitudes.

35 The strong near-field signal peak was ~~suppressed-attenuated~~ by using a narrow aperture and by rotating the laser
36 beam away from the telescope axis. However, this resulted in a slightly reduced overlap as far as almost 20 km,
37 as can be seen in the temperature data (Fig. 202). The combined raw data were smoothed with a VDI vertical
38 resolution scaling as shown in Fig. 24-19, the maximum value staying below 2 km.

39 The temperature data were initialized at 87 km a.s.l. (density: at 95 km) by using the temperature of the U.S.
40 Standard atmosphere as the start value. The performance is surprisingly good, despite the strongly growing noise

1 of the raw data in this altitude range. The agreement with the temperatures from the Munich radiosonde and
2 NCEP is very good up to the upper end of the NCEP table (50 km) downloaded from the NDACC web site. For
3 higher altitudes we first compared our results with the MSIS model output calculated for our site, as
4 recommended by Wing et al. (2018). There is a strong discrepancy that could not be reduced by selecting the
5 MSIS temperature at 87 km as the start value of the retrieval: The temperature converged to the curve for the
6 standard atmosphere within just 15 km.

7 A comparison with the temperature of the Microwave Limb Sounder (MLS) during the early hours of 16
8 November for a position 3.5° farther to the east. Considering the difference in position the agreement with the
9 MLS temperature profile is quite good, with a strong similarity in structure. The temperature peak at 65 km is
10 present, but slightly downward shifted.

11 In summary we are highly satisfied by this first result [for a wide-range temperature measurement](#). In principle,
12 due to the very small average background signal, Poisson effects in the photon statistics must be taken into
13 consideration. More advanced approaches are needed, such as that presented by Sica and Haefele (2016).

14 **7 Discussion and Conclusions**

15 The primary goals of the system development described in this paper have been to reduce the measurement time
16 for lower-stratospheric water vapour up to at least 20 km to one hour and to achieve temperature measurements
17 up to more than 80 km. These goals have been met, with a satisfactory performance. Nevertheless, a comparison
18 with the simulations in Sect. 4.4 clearly shows that the measured lidar signal for water vapour is considerably
19 smaller than predicted.

20 At 15 km our measurements typically yield H₂O Raman returns of 2 counts per 7.5-m bin and hour. This is
21 converted to 53 counts for the 200-m bins used in the calculation [in Sect. 4.4](#), one sixth of the 315 counts
22 simulated. Roughly a factor of two is due to the lower laser power in comparison with the 200 W assumed in the
23 simulation. For the rest, apart from uncertainties in the parameters used in the numerical estimate, we found that
24 the most likely reason for this discrepancy is that the Raman cross section used in the calculations is presumably
25 given for the sum of all three ro-vibrational branches. Indeed, the peak signal increased by roughly a factor of
26 three when we removed the 347-nm interference filter, which includes the missing attenuation by the
27 interference filter ($T = 0.72$).

28 As a consequence, we carried out measurements without interference filter. However, this resulted in a much
29 higher stratospheric mixing ratio of 120 ppm due to insufficient blocking of 308- or 332-nm radiation. Thus, for
30 collecting the signal from the entire ro-vibrational band at least a broad-band interference filter (bandwidth 20
31 nm) must be added to reject residual contributions from the other channels and to reduce the observed 3 to 4
32 background counts.

33 The background is dominated by the size of the entrance slit. The optimum slit width is different for both lasers,
34 given different beam divergences. Therefore, in the future two additional slits will be used in focal points of the
35 347-nm and 355-nm channels (Fig. 97). These slits are easier accessible than the entrance slit which facilitates to
36 optimize their position and size.

37 There are obvious possibilities to enhance the laser power. Better transmitting intracavity optics should be
38 installed for significantly reducing the thermal load. A higher transmittance would, therefore, also allow us to
39 remove the cylindrical telescope (Fig. 3) that was introduced to reduce the intracavity intensity on the optical
40 components added by us. As a consequence, the resonator would become shorter and the number of cavity round

1 trips within the fluorescence time of XeCl would grow. As pointed out in Sect. 2.1 the reduction of the numbers
2 of round trips is likely to be the dominant loss factor in the extended resonator.

3 The calibration of the water-vapour channel was confirmed to be a key issue for the long-term operation of the
4 lidar. We hope that the UFS DIAL can soon be re-activated for filling this gap. Additional control by inspecting
5 the data from surrounding radiosonde stations or the signal level at 308 nm and 332 nm are other important tools
6 to ensure long-term stability of the system. A longer comparison with CFH sensors than in the campaign in
7 February 2019 would also be advantageous. This would be particularly important during periods with
8 fluorescing aerosol in the lower stratosphere in order to assess the influence of this kind of background at 347
9 nm.

10
11 The temperature measurements with a separate, frequency-tripled Nd:YAG laser were quite successful.
12 Improvements could result from using a diode-pumped Nd:YAG laser with 300 or 350 Hz repetition rate,
13 matching that of the XeCl laser. Such lasers are meanwhile available. We expect lower pulse energies for such a
14 laser at 355 nm, but the currently available 160 mJ yielded too much backscatter signal anyway.

15 The remaining ~~effortstasks~~ will concentrate on testing the rotational Raman channels with the new spectral
16 filters, on implementing the ozone correction (not possible for the configuration with 353 nm) and on completing
17 the remote control of the lidar system. Automatic control of the alignment is the key to more frequent
18 measurements, intensifying the measurements. Lidar measurements at high temporal resolution may yield
19 ~~important hints~~more information on the role of atmospheric transport, in particular TST, on the water vapour
20 concentration in the UTLS. Finally, ~~given the current debate on the climate development, an important~~
21 ~~contribution to the question about the H₂O feedback could be given~~we head for long-term operation of the
22 system with stable performance in order to provide insight into the H₂O feedback in the climate system.

Irupdlhu#ihjhvwhoow

24 5 Data availability

25 Data can be obtained on request from several authors of this paper (christian.rolf@fzj.de; thomas@trickl.de,
26 hannes.vogelmann@kit.de).

27 6 Author statement

28 All authors from Garmisch-Partenkirchen were involved in system development and lidar testing. The Jülich
29 team launched balloons at IMK-IFU.

30 7 Competing interests

31 The authors declare that they have no conflict of interest.
32

33 Acknowledgements

34 The authors thank Hans Peter Schmid for his interest and support. They are indebted to Werner Funk, Bernd
35 Mielke, Heinz Josef Romanski and Bernhard Stein for numerous important discussions and technical
36 improvements. Stuart McDermid sent valuable information on the feasibility of Raman lidar measurements of
37 H₂O in the stratosphere which encouraged us to start this project. We strongly appreciate the intense discussions
38 with our NDACC colleagues. Wolfgang Steinbrecht generously made available results from the nearby

1 Hohenpeißenberg observatory, Gerald Nedoluha provided the MLS reference data. The good co-operation with
2 the Coherent team in Göttingen was crucial for the laser upgrading. Also crucial has been the excellent help by
3 Werner Moorhoff and Laseroptik who made numerous attempts for optimizing the performance of their
4 dielectric coatings. In particular, their tenacity in optimizing the reflectance of the large mirrors in the transmitter
5 at their own costs this project prevented serious damage to this project. This work has been funded by the
6 Bavarian State Ministry of Environment and Consumer Protection under contracts 45001226 (KIT), TLK01U-
7 49581 and VAO-II TPI/01. KIT acknowledges support of lidar measurements by the European Space Agency
8 (ESA) under Contract 4000123691/18/NL/NF (FIRMOS validation campaign). Balloon profiles utilized in this
9 paper have been provided within the same ESA project by the Forschungszentrum Jülich via subcontract with
10 KIT. The balloon activities were also partly supported by the Helmholtz Association in the framework of
11 MOSES (Modular Observation Solutions for Earth Systems).

12 The service charges for this open-access publication have been covered by a Research Centre of the Helmholtz
13 Association.

14 **References**

- 15 Arshinov, Y. F., Bobrovnikov, S. M., Zuev, V. E., and Mitev, V. M.: Atmospheric temperature measurements
16 using a pure rotational Raman lidar, *Appl. Opt.*, 22, 2984-2990, 1983.
- 17 Avila, G., Fernandez, J. M., Tejada, G., and Montero, S.: The Raman spectra and cross-sections of H₂O D₂O,
18 and HDO in the OH/OD stretching regions, *J. Mol. Spectrosc.*, 228, 38-65, 2004.
- 19 Barnes, J. E., Kaplan, T., Vömel, H., and Read, W. G.: NASA/Aura/Microwave Limb Sounder water vapor
20 validation at Mauna Loa Observatory by Raman lidar, 113, D15S03, doi:10.1029/2007JD008842, 5 pp., 2008.
- 21 Brabec, M.: Backscatter and Humidity Measurements in Cirrus and Dust Clouds using Balloon Sondes, Ph.D.
22 thesis, Eidgenössische Technische Hochschule, Zürich (Switzerland), 96 pp., 2011.
- 23 Bragg, S. L., Brault, J. W., and Smith, W. H.: Line Positions and Strengths in the H₂ Quadrupole Spectrum,
24 *Astrophys. J.*, 263, 999-1004, 1982.
- 25 Broadfoot, A. L., and Kendall, K. R.: The Airglow Spectrum, 3100 – 10,000 Å, *J. Geophys. Res.*, 73, 426-428,
26 1968.
- 27 Carnuth, W., and Trickl, T.: A powerful eyesafe infrared aerosol lidar: application of stimulated Raman
28 backscattering of 1.06 µm radiation, *Rev. Sci. Instrum.*, 65, 3324-3331, 1994.
- 29 Chen, B., and Liu, Z.: Global water vapor variability and trend from the latest 36 year (1979 to 2014) data of
30 ECMWF and NCEP reanalyses, radiosonde, GPS, and microwave satellite, *J. Geophys. Res.*, 121, 11,442–
31 11,462, doi:10.1002/2016JD024917, 2016.
- 32 Congeduti, F., Marengo, F., Baldetti, P., and Vicenti, E.: The multiple lidar '9-eyes', *J. Opt. A*, 1, 185-191, 1999.
- 33 Deuber, B., Kämpfer, N., Feist, D. G.: A New 22-GHz Radiometer for Middle Atmospheric Water Vapor Profile
34 Measurements, *IEEE Transactions on Geoscience and Remote Sensing*, 42, 974-984, 2004.
- 35 Deuber, B., Haefele, A., Feist, D. G., Martin, L., Nedoluha, G. E., Yushkov, V., Khaykin, S., Kivi, R., and
36 Vömel, H.: Middle Atmospheric Water Vapour Radiometer (MIAWARA): Validation and first results of the
37 LAPBIAT Upper Tropospheric Lower Stratospheric Water Vapor Validation Project (LAUTLOS-WAVVAP)
38 campaign, *J. Geophys. Res.*, 110, D13306, doi: 10.1029/2004JD005543, 10 pp., 2005.
- 39 Dickenson, G. D., Niu, M. L., Salumbides, E. J., Komasa, J., Eikema, K. S. E., Pachucki, K., and Ubachs, W.:
40 Fundamental Vibration of Molecular Hydrogen, *Phys. Rev. Lett.*, 110, 193601, 5 pp., 2013.

1 Dionisi, D., Congeduti, F., Liberti, G. L., and Cardillo, F.: Calibration of a Multichannel Water Vapor Raman
2 Lidar through Noncollocated Operational Soundings: Optimization and Characterization of Accuracy and
3 Variability, *J. Atmos. Oceanic Technol.*, 27, 108-121, 2010.

4 Dionisi, D., Liberti, G. L., and Congeduti, F.: Variable Integration Domain technique for Multichannel Raman
5 Water Vapour Lidar Measurements, in: Reviewed and Revised Papers Presented at the 26th International Laser
6 Radar Conference (ILRC 2012), Porto Heli (Greece), A. Papayannis, D. Balis, V. Amiridis, Eds., published in
7 Greece on behalf of the International Co-ordination Group for Laser Atmospheric Studies (ICLAS), 861-864,
8 2012; system description in Ref. 41

9 Dionisi, D., Keckhut, P., Courcoux, Y., Hauchecorne, A., Porteneuve, J., Baray, J. L., Leclair de Bellevue, J.,
10 Vèrèmes, H., Gabarrot, F., Payen, G., Decoupes, R., and Cammas, J. P.: Water vapor observations up to lower
11 stratosphere through the Raman lidar during the Maïdo Lidar Calibration Campaign, *Atmos. Meas. Tech.*, 8,
12 1425-1445, 2015.

13 Dirksen, R. J., Sommer, M., Immler, F. J., Hurst, D. F., Kivi, R., and Vömel, H.: Reference quality upper-air
14 measurements: GRUAN data processing for the Vaisala RS92 radiosonde, *Atmos. Meas. Tech.*, 7, 4463-4490,
15 doi.org/10.5194/amt-7-4463-2014, 2014.

16 Draxler, R., and Hess, G.: An overview of the HYSPLIT_4 modelling system for trajectories, dispersion, and
17 deposition, *Aust. Meteorol. Mag.*, 47, pp. 295-308, 1998.

18 [Gettelman, A., Hoor, P., Pan, L. L., Randel, W. L., Hegglin, M. I., and Birner, T.: The Extratropical Upper](#)
19 [Troposphere and Lower Stratosphere, *Rev. Geophys.*, 49, RG3003, doi: 10.1029/2011RG000355, 31 pp., 2011.](#)

20 Golubiatnikov, G. Y., and Krupnov, A. F.: Molecular constants of the ground state of oxygen (¹⁶O₂) accounting
21 for new experimental data, *J. Mol. Spectrosc.*, 225, 222-224, 2004.

22 Han, Y., and Westwater, E. R.: Remote Sensing of Tropospheric Water Vapor and Cloud Liquid Water by
23 Integrated Ground-Based Sensors, *J. Atmos. Oceanic Technol.*, 12, 1050-1059, 1995.

24 Hauchecorne, A., and Chanin, M.-L.: Density and Temperature Profiles Obtained by Lidar between 33 and 70
25 km, *Geophys. Res. Lett.*, 7, 565-568, 1980.

26 Hegglin, M. I., Plummer, D. A., Shepherd, T. G., Scinocca, J. F., Anderson, J., Froidevaux, L., Funke, B., Hurst,
27 D., Rozanov, A., Urban, J., von Clarmann, T., Walker, K. A., Wang, H. J., Tegtmeier, S., and Weigel, K.:
28 Vertical structure of stratospheric water vapour trends derived from merged satellite data, *Nature Geoscience*, 7,
29 768-776, 2014.

30 Hints, E. J., Weinstock, E. M., Anderson, J. G., May, R. D., and Hurst, D. F.: On the accuracy of in situ water
31 vapor measurements in the troposphere and lower stratosphere with Harvard Lyman- α hygrometer, *J. Geophys.*
32 *Res.*, 104, 8183-8189, 1999.

33 Hocke, K., and Martin, L.: Monitoring Atmospheric Water Vapour, International Space Science Institute, Bern
34 (Switzerland), ISSI Scientific Reports Series, Vol. 10, Springer (New York, Dordrecht, Heidelberg, London),
35 ISBN 978-1-4614-3908-0, 326 pp., 2013.

36 Höveler, K.: Entwicklung eines Nahbereichsempfängers zur Messung von Wasserdampf- und
37 Temperaturprofilen für das Hochleistungs-Raman-Lidar am Schneefernerhaus, Masterarbeit, Karlsruher Institut
38 für Technologie, Fakultät für Physik, 138 pp., 2015 (in German).

39 Hurst, D. F., Oltmans, S. J., Vömel, H., Rosenlof, K. H., Davis, S. M., Ray, E. A., Hall, E. G., and Jordan, A. F.:
40 Stratospheric water vapor trends over Boulder, Colorado: Analysis of the 30 year Boulder record, *J. Geophys.*
41 *Res.*, 116, D02306, doi: 10.1029/2010JD015065, 12 pp., 2011.

1 Hurst, D. F., Read, W. G., Vömel, H., Selkirk, H. B., Rosenlof, K. H., Davis, S. M., Hall, E. G., Jordan, A. F.,
2 and Oltmans, S. J.: Recent divergences in stratospheric water vapor measurements by frost point hygrometers
3 and the Aura Microwave Limb Sounder, *Atmos. Meas. Tech.*, 9, 4447-4457, 2016.

4 [Immler, F., Engelbart, D., and Schrems, O.: Fluorescence from atmospheric aerosol detected by lidar indicates
5 biogenic particles in the lowermost stratosphere. *Atmos. Chem. Phys.*, 5, 345-355, 2005.](#)

6 Jensen, E. J., Ackermann, A. S., and Smith, J. A.: Can overshooting convection dehydrate the tropical
7 tropopause layer? *J. Geophys. Res.*, 112, D11209, doi: 10.1029/2006JD007943, 5 pp., 2007.

8 Johnston, J. E., and Broadfoot, A. L.: Midlatitude Observations of the Night Airglow: Implications to Quenching
9 Near the Mesopause, *J. Geophys. Res.*, 98, 21593-21603, 1993.

10 Kämpfer, N. (Ed.), Smit, H., Kivi, R., Paukkunen, A., Vömel, H., Jeannot, P., Youshkov, V., Nedoluha, G.,
11 Haefele, A., De Wachter, E., Schneider, M., Demoulin, P., Sussmann, R., Notholt, J., Leblanc, T., Trickl, T.,
12 Vogelmann, H., Braathen, G. O., Urban, J., Lambert, J.-C., International Space Science Institute, Bern
13 (Switzerland), ISSI Scientific Reports Series, Vol. 10, ISBN 978-1-4614-3908-0, Springer (Berlin, Heidelberg,
14 New York), 326 pp., 2013.

15 Khattatov, V., Yushkov, V., Kaplanov, M., Zaitzev, I., Rosen, J., and Kjöme, N.: Some results of water vapor,
16 ozone and aerosol balloon borne measurements during EASOE, *Geophys. Res. Lett.*, 21, 1299-1302, 1994.

17 Kempfer, U., Carnuth, W., Lotz, R., and Trickl, T.: A wide range ultraviolet lidar system for tropospheric ozone
18 measurements: development and application, *Rev. Sci. Instrum.*, 65, 3145-3164, 1994.

19 Kiehl J. T., and Trenberth, K. E.: Earth's Annual Global Mean Energy Budget, *Bull Am. Met. Soc.*, 78, 197-208,
20 1997.

21 Klanner, L., Trickl, T. and Vogelmann, H.: On the Way to Combined DIAL and Raman-Lidar Sounding of
22 Water Vapour on Mt. Zugspitze – a Progress Report, in: Reviewed and Revised Papers Presented at the 26th
23 International Laser Radar Conference (ILRC 2012), Porto Heli (Greece, [2012](#)), ~~25 to 29 June 2012~~, A.
24 Papayannis, D. Balis, V. Amiridis, Eds., published in Greece on behalf of the International Co-ordination Group
25 for Laser Atmospheric Studies (ICLAS), 853-826, 2012.

26 [L. Klanner, T. Trickl, H. Vogelmann, Water-vapour measurements up to the lower stratosphere — the high
27 power Raman lidar at the Schneefernerhaus, 28th International Laser Radar Conference, Bucharest \(Romania,
28 2017\), EPJ Web of Conferences, 176, 01026, DOI: <https://doi.org/10.151/epjconf/201817601026>, 4 pp., 2018.](#)

29 Klett, J. D.: Stable analytical inversion solution for processing lidar returns, *Appl. Opt.*, 20, 211-220, 1981.

30 Klett, J. D.: Lidar inversion with variable backscatter/extinction ratios, *Appl. Opt.*, 24, 1638-1643, 1985.

31 Kley, D., and E. J. Stone, E. J.: Measurement of water vapor in the stratosphere by photodissociation with Ly α
32 (1216 Å) light, *Rev. Sci. Instrum.*, 49, 691-697, 1978.

33 Kneizys, F. X., Anderson, G. P., Shettle, E. P., Gallery, W. O., Abreu, L. W., Selby, J. E. A., Chetwynd, J. H.,
34 and Clough, S. A.: Users guide to LOWTRAN 7, Rep. AFGL-TR-88-0177, Environ. Res. Pap., 1010, 1988.

35 Kreipl, S.: Messung des Aerosoltransports am Alpennordrand mittels Laserradar (Lidar), Dissertation, Friedrich-
36 Alexander-Universität Erlangen-Nürnberg (Germany), 195 pp., 2006; in German.

37 Kung, A.H., Trickl, T., Gershenfeld, N. A., and Lee, Y. T.: State-selective Detection of H₂ by 1 + 1 REMPI via
38 the C ¹Πu (v' = 0, J') States, *Chem. Phys. Lett.*, 144, 427-430, 1988.

Irupdwlhuh#qjolv#yuhlqlj#vqljuhlfk,

Irupdwlhuh#kfkjhvwhoow

Irupdwlhuh#kuliw#u#k#hww

Ihogixqnlw#h#fiqghuw

1 Lacis, A. A., Hansen, J. E., Russell, G. L., Oinas, V., and Jonas, J.: The role of long-lived greenhouse gases as
2 principal LW control knob that governs the global surface temperature for past and future climate change, *Tellus*
3 *B*, 65, 19734, doi:10.3402/tellusb.v65i0.19734, 25 pp., 2013.

4 Leblanc, T., and McDermid, I. S.: Accuracy of Raman lidar water vapor calibration and its applicability to long-
5 term measurements, *Appl. Opt.*, 47, 5592-5603, 2008.

6 Leblanc, T., and McDermid, I. S.: Reply to “Comments on “Accuracy of Raman lidar water vapor calibration
7 and its applicability to long-term measurements””, *Appl. Opt.*, 50, 2177-2178, 2011.

8 Leblanc, T., McDermid, I. S., and Walsh, T. D.: Ground-based water vapor Raman lidar measurements up to
9 upper troposphere and lower stratosphere for long-term monitoring, *Atmos. Meas. Tech.*, 5, 17-36, 2012.

10 ~~Leblanc, T., and McDermid, I. S.: Accuracy of Raman lidar water vapor calibration and its applicability to long-~~
11 ~~term measurements, Appl. Opt., 47, 5592-5603, 2008.~~

12 ~~Leblanc, T., and McDermid, I. S.: Reply to “Comments on “Accuracy of Raman lidar water vapor calibration~~
13 ~~and its applicability to long-term measurements””, Appl. Opt., 50, 2177-2178, 2011.~~

14 Leblanc, T., Sica, R. J., van Gijssel, J. A. E., Godin-Beekmann, S., Haeferle, A., Trickl, T., Payen, G., and
15 Gabarrot, F.: Proposed standardized definitions for vertical resolution and uncertainty in the NDACC lidar ozone
16 and temperature algorithms. Part 1: Vertical resolution, *Atmos. Meas. Tech.*, 9, 4029-4049, 2016; 18-pp.
17 supplement

18 ~~Luo, B. P., Peter, T., Wernli, H., Fueglistaler, S., Wirth, M., Kiemle, C., Flentje, H., Yushkov, V. A., Khattatov,~~
19 ~~V., Rudakov, V., Thomas, A., Borrmann, S., Toci, G., Mazzinghi, P., Beuermann, J., Schiller, C., Cairo, F., Di-~~
20 ~~Donfrancesco, G., Adriani, A., Volk, C. M., Strom, J., Noone, K., Mitev, V., MacKenzie, R. A., Carslaw, K. S.,~~
21 ~~Trautmann, T., Santacesaria, V., and Stefanutti, L.: Ultrathin Tropical Tropopause Clouds (UTTCs): II.~~
22 ~~Stabilization mechanism, Atmos. Chem. Phys., 23, 1083-1091, 2003.~~

23 McDermid, I. S., Haner, D. A., Kleiman, M. M., Walsh, T. D., and White, M. L.: Differential absorption lidar
24 systems for tropospheric and stratospheric ozone measurements, *Opt. Eng.*, 30, 22-30, 1991.

25 Mieruch, S., Noël, S., Bovensmann, H., and Burrows, J. P.: Analysis of global water vapour trends from satellite
26 measurements in the visible spectral range, *Atmos. Chem. Phys.*, 8, 491-504, 2008.

27 Miloshevich, L. M., Vömel, H., Whiteman, D. N., Lesht, B. M., Schmidlin, F. J., and Russo, F.: Absolute
28 accuracy of water vapor measurements from six operational radiosonde types launched during AWEX-G and
29 implications for AIRS validation, *J. Geophys. Res.*, 111, D09S10, doi: 10.1029/2005JD006083, 25 pp., 2006.

30 Mohr, P. J., Newell, D. B., and Taylor, B. N.: CODATA Recommended Values of the Fundamental Physical
31 Constants: 2014, National Institute of Standards and Technology, Gaithersburg (Maryland, U.S.A.),
32 <https://arxiv.org/pdf/1507.07956.pdf>, 11 pp., 2014.

33 Müller, R., Kunz, A., Hurst, D. F., Rolf, C., Krämer, M., and Riese, M.: The need for accurate long-term
34 measurements of water vapor in the upper troposphere and lower stratosphere with global coverage, *Earth's*
35 *Future*, 4, 25-32, 2016.

36 Nedoluha, G. E., Bevilacqua, R. M., Gomez, R. M., Waltman, W. B., Hicks, B. C., Thacker, D. L., Russell III, J.
37 M., Abrams, M., Pumphrey, H. C., and Connor, B. J.: A comparative study of mesospheric water vapor
38 measurements from the ground-based water vapor millimeter-wave spectrometer and space-based instruments, *J.*
39 *Geophys. Res.*, 102, 16647-16661, 1997.

1 Peter, T., Luo, B. P., Wirth, M., Kiemle, C., Flentje, H., Yushkov, V. A., Khattatov, V., Rudakov, V., Thomas,
2 A., Borrmann, S., Toci, G., Mazzinghi, P., Beuermann, J., Schiller, C., Cairo, F., Di Donfrancesco, G., Adriani,
3 A., Volk, C. M., Strom, J., Noone, K., Mitev, V., MacKenzie, R. A., Carslaw, K. S., Trautmann, T.,
4 Santacesaria, V., and Stefanutti, L.: Ultrathin Tropical Tropopause Clouds (UTTCs): I. Cloud morphology and
5 occurrence, *Atmos. Chem. Phys.*, 23, 1083-1091, 2003.

6 ~~Luo, B. P., Peter, T., Wernli, H., Fueglistaler, S., Wirth, M., Kiemle, C., Flentje, H., Yushkov, V. A., Khattatov,
7 V., Rudakov, V., Thomas, A., Borrmann, S., Toci, G., Mazzinghi, P., Beuermann, J., Schiller, C., Cairo, F., Di-
8 Donfrancesco, G., Adriani, A., Volk, C. M., Strom, J., Noone, K., Mitev, V., MacKenzie, R. A., Carslaw, K. S.,
9 Trautmann, T., Santacesaria, V., and Stefanutti, L.: Ultrathin Tropical Tropopause Clouds (UTTCs): II.
10 Stabilization mechanism, *Atmos. Chem. Phys.*, 23, 1083-1091, 2003.~~

11 Paltridge, G., Arking, A., and Pook, M.: Trends in middle- and upper-level tropospheric humidity from NCEP
12 reanalysis data, *Theor. Appl. Climatol.*, 98, 351–359, 2009.

13 ~~Pan, L. L., Bowman, K. P., Shapiro, M., Randel, W. J., Gao, R. S., Campos, T., Davis, C., Schauffler, S., Ridley,
14 B. A., Wei, J. C., and Barnett, C.: Chemical behavior of the tropopause observed during the Stratosphere-
15 Troposphere Analyses of Regional Transport experiment, *J. Geophys. Res.*, 112, D18110, doi:
16 10.1029/2007JD008645, 13 pp., 2007.~~

17 Perrone, M. R., and Piccinno, V.: On the benefits of astigmatic focusing configurations in stimulated Raman
18 scattering processes, *Opt. Comm.*, 133, 534-540, 1997.

19 ~~Reichardt, J., Leinweber, R., and Schwebe, A.: Fluorescing Aerosols and Clouds: Investigations of Co-existence,
20 28th International Laser Radar Conference, Bucharest (Romania, 2017), *EPJ Web of Conferences* 176, 05010,
21 <https://doi.org/10.1051/epjconf/201817605010>, 4 pp., 2018.~~

22 Rosenlof, K. H.: How Water Enters the Stratosphere, *Science*, 302, 169-170, 2003.

23 Ross, R.J., and Elliott, W. P.: Radiosonde-Based Northern Hemisphere Tropospheric Water Vapor Trends, *J.*
24 *Climate*, 14, 1602–1612, 2001.

25 Rouillé, G., Millot, G., Saint-Loup, R., and Berger, H.: High-Resolution Stimulated Raman Spectroscopy of O₂,
26 *J. Mol. Spectrosc.*, 154, 372-382, 1992.

27 Scherer, M., Vömel, H., Fueglistaler, S., Oltmans, S. J., and Stachelin, J.: Trends and variability of midlatitude
28 stratospheric water vapour deduced from the re-evaluated Boulder balloon series and HALOE, *Atmos. Chem.*
29 *Phys.*, 8, 1391–1402, 2008.

30 Schmidt, G. A., Ruedy, R. A., Miller, R. L., and Lacis, A. A.: Attribution of the present-day total greenhouse
31 effect, *J. Geophys. Res.*, 115, D20106, doi:10.1029/2010JD014287, 6 pp. 2010.

32 Shibata, T., Kobuchi, M., and Maeda, M.: Measurements of density and temperature profiles in the middle
33 atmosphere with a XeF lidar, *Appl. Opt.*, 25, 685-688, 1986.

34 Sica, R. J., and Haeferle, A.: Retrieval of temperature from a multiple-channel Rayleigh-scatter lidar using an
35 optimal estimation method, *Appl. Opt.*, 54, 1872-1889, 2015.

36 Smit, H. G. J., Straeter, W., Johnson, B. J., Oltmans, S. J., Davies, J., Tarasick, D. W., Hoegger, B., Stubi, R.,
37 Schmidlin, F. J., Northam, T., Thompson, A. M., Witte, J. C., Boyd, I., and Posny, F.: Assessment of the
38 Performance of ECC-ozonesondes under Quasi-flight Conditions in the Environmental Simulation Chamber:
39 Insights from the Jülich Ozone Sonde Intercomparison Experiment (JOSIE), *J. Geophys. Res.*, 112, D19306,
40 doi:10.1029/2006JD007308, 18 pp., 2007.

Irupdwluh#qjolv#kzhuhqlj#ivqljuhlfk,
Irupdwluh#qjolv#kzhuhqlj#ivqljuhlfk,
Irupdwluh#kfkjhvwwhoow
Irupdwluh#qjolv#kzhuhqlj#ivqljuhlfk,

1 Solheim, F., and Godwin, J. R.: Passive ground-based remote sensing of atmospheric temperatur, water vapor,
2 and cloud liquid water profiles by a frequency synthesized microwave radiometer, *Meteorol. Z.*, 7, 370-376,
3 1998.

4 Solomon, S., Rosenlof, K. H., Portmann, R. W., Daniel, J. S., Davis, S. M., Sanford, T. J., and Plattner, G.-K.:
5 Contributions of Stratospheric Water Vapor to Decadal Changes in the Rate of global warming, *Science*, 327,
6 1219-1223, 2010.

7 Stein, A. F., Draxler, R. R., Rolph, G. D., Stunder, B. J. B., Cohen, M. D., and Ngan, F.: NOAA's HYSPLIT
8 atmospheric transport and dispersion modeling system, *Bull. Amer. Meteor. Soc.*, 96, 2059-2077, 2015.

9 Steinbrecht, W., Claude, H., Schönnenborn, F., Leiterer, U., Dier, H., and Lanzinger, E., Pressure and
10 Temperature Differences between Vaisala RS80 and RS92 Radiosonde Systems", *J. Atmos. Oceanic Technol.*,
11 25, 909-927, 2008.

12 [Stohl, A., and Trickl, T.: A textbook example of long-range transport: Simultaneous observation of ozone](#)
13 [maxima of stratospheric and North American origin in the free troposphere over Europe. *J. Geophys. Res.*, 104,](#)
14 [30445-30462, 1999.](#)

15 Stohl, A.: A 1-year Lagrangian "climatology" of airstreams in the Northern Hemisphere troposphere and
16 lowermost stratosphere, *J. Geophys. Res.*, 106, 7263–7279, 2001.

17 Stohl, A., Bonasoni, P., Cristofanelli, P., Collins, W., Feichter, J., Frank, A., Forster, C., Gerasopoulos, E.,
18 Gäggeler, H., James, P., Kentarchos, T., Kromp-Kolb, H., Krüger, B., Land, C., Meloen, J., Papayannis, A.,
19 Priller, A., Seibert, P., Sprenger, M., Roelofs, G. J., Scheel, H. E., Schnabel, C., Siegmund, P., Tobler, L., Trickl,
20 T., Wernli, H., Wirth, V., Zanis, P., and Zerefos, C.: Stratosphere-troposphere exchange - a review, and what we
21 have learned from STACCATO, *J. Geophys. Res.*, 108, 8516, doi:10.1029/2002JD002490, STA 1, 15 pp., 2003.

22 Trickl, T.: Upgraded 1.56- μm lidar at IMK-IFU with 0.28 J/pulse", *Appl. Opt.*, 49, 3732-3740, 2010.

23 Trickl, T., and Wanner, J.: The dynamics of the reactions $F + IX \rightarrow IF + X$ ($X = Cl, Br, I$); a laser-induced
24 fluorescence study, *J. Chem. Phys.*, 78, 6091-6101, 1983.

25 Trickl, T., and Wanner, J.: $IF(A \rightarrow X, B \rightarrow X)$ chemiluminescence from the $F + I_2F$ reaction, *J. Chem. Phys.*, 74,
26 6508-6510, 1981; repeated with reduced noise: Trautmann, M., Trickl, T., and Wanner, J.: $IF(A \rightarrow X, B \rightarrow X)$
27 Chemiluminescence of Fluorine-iodide Systems in a Crossed Molecular Beam Experiment, in: "Selectivity in
28 Chemical Reactions", NATO Advanced Science Institute Series, Series C (Mathematical and Physical Sciences),
29 Vol. 245, Proceedings of the NATO Advanced Workshop in Bowes-on-Windermere (Great Britain), Sep. 7 to
30 11, 1987, J. C. Whitehead, Ed., Kluwer Academic Publishers (Dordrecht, The Netherlands), 525-529, 1988;
31 <http://www.trickl.de/NATO1988.pdf>.

32 Trickl, T., Proch, D., and Kompa, K. L.: Resonance-Enhanced 2 + 2 Photon Ionization of Nitrogen: The Lyman-
33 Birge-Hopfield Band System, *J. Mol. Spectrosc.*, 162, 184-229, 1993.

34 Trickl, T., Proch, D., and Kompa, K. L.: The Lyman-Birge-Hopfield System of Nitrogen: Revised Calculation of
35 the Energy Levels, *J. Mol. Spectrosc.*, 171, 374-384, 1995.

36 Trickl, T., Feldmann, H., Kanter, H.-J., Scheel, H. E., Sprenger, M., Stohl, A., and Wernli, H.: Deep
37 stratospheric intrusions over Central Europe: case studies and climatological aspects, *Atmos. Chem. Phys.*, 10,
38 499-524, 2010a.

Irupdwlhuvkuliw@kwhw

1 Trickl, T., Kung, A. H., and Lee, Y. T.: A Pulsed Source of Cold Hydrogen and Hydrogen Clusters:
2 Development and Extreme-ultraviolet Studies, *Appl. Phys. B*, 101, 321-335, 2010**b**; the detection sensitivity for
3 H₂ was enhanced by orders of magnitude with respect to the 1.7×10⁵ cm⁻³ of Kung et al. (1988).

4 Trickl, T., Giehl, H., Jäger, H., and Vogelmann, H.: 35 years of stratospheric aerosol measurements at Garmisch-
5 Partenkirchen: from Fuego to Eyjafjallajökull, and beyond, *Atmos. Chem. Phys.*, 13, 5205-5225, 2013.

6 Trickl, T., Vogelmann, H., Giehl, H., Scheel, H. E., Sprenger, M., and Stohl, A.: How stratospheric are deep
7 stratospheric intrusions? *Atmos. Chem. Phys.*, 14, 9941-9961, 2014.

8 Trickl, T., Vogelmann, H., Flentje, H., and Ries, L.: Stratospheric ozone in boreal fire plumes – the 2013 smoke
9 season over Central Europe, *Atmos. Chem. Phys.*, 15, 9631-9649, 2015.

10 Trickl, T., Vogelmann, H., Fix, A., Schäfler, A., Wirth, M., Calpini, B., Levrat, G., Romanens, G., Apituley, A.,
11 Wilson, K. M., Begbie, R., Reichardt, J., Vömel, H. and Sprenger, M.: How stratospheric are deep stratospheric
12 intrusions into the troposphere? LUAMI 2008, *Atmos. Chem. Phys.*, 16, 8791-8815, 2016.

13 Trickl, T., Vogelmann, H., Ries, L., and Sprenger, M.: Very high stratospheric influence observed in the free
14 troposphere over the Northern Alps – just a local phenomenon? *Atmos. Chem. Phys.*, 20, 243-266, 2020**a**.

15 Trickl, T., Neidl, F., Giehl, H., Perfahl, M., and Vogelmann, H.: Three decades of tropospheric ozone lidar
16 development at Garmisch-Partenkirchen, *Atmos. Meas. Tech.*, ~~Disse.~~, AMT-2020-89, in press, 2020b.

17 U.S. Standard Atmosphere 1976, National Oceanic and Atmospheric Organization (NOAA), National
18 Aeronautics and Space Administration, United States Air Force, NOAA-S/T 76-1562, U.S. Printing Office
19 (Washington, D.C.), 227 pp., 1976.

20 Vaisala: Vaisala Radiosonde RS41 Measurement Performance, White Paper, Vaisala, Helsinki (Finland),
21 [https://www.vaisala.com/sites/default/files/documents/WEA-MET-RS41-Performance-White-paper-](https://www.vaisala.com/sites/default/files/documents/WEA-MET-RS41-Performance-White-paper-B211356EN-B-LOW-v3.pdf)
22 [B211356EN-B-LOW-v3.pdf](https://www.vaisala.com/sites/default/files/documents/WEA-MET-RS41-Performance-White-paper-B211356EN-B-LOW-v3.pdf), 28 pp., 2017.

23 VDI guide line 4210, Remote sensing, Atmospheric measurements with LIDAR, Measuring gaseous air
24 pollution with the DAS LIDAR, Verein Deutscher Ingenieure (Düsseldorf, Germany), pp. 47, 1999.

25 Vèrèmes, H., Payen, G., Keckhut, P., Dufлот, V., Baray, J.-L., Cammas, J.-P., Evan, S., Posny, F., Körner, S.,
26 and Bosser, P.: Validation of the Water Vapor Profiles of the Raman Lidar at the Maïdo Observatory (Reunion
27 Island) Calibrated with Global Navigation Satellite System Integrated Water Vapor, *Atmosphere*, 10, 713,
28 doi:10.3390/atmos10110713, 21 pp., 2019.

29 Vömel, H., Selkirk, H., Miloshevich, L., Valverde-Canossa, J., Valdés, J., Kyro, E., Kivi, R., Stolz, W., Peng,
30 G., and Diaz, J. A., Radiation Dry Bias of the Vaisala RS92 Humidity Sensor, *J. Atmos. Oceanic Technol.*, 24,
31 953-963, 2007a.

32 Vömel, H., David, D. E., and Smith, K.: Accuracy of tropospheric and stratospheric water vapor measurements
33 by the cryogenic frost point hygrometer: Instrumental details and observations, *J. Geophys. Res.*, 112, D08305,
34 doi: 10.1029/2006JD007224, 14 pp., 2007b.

35 Vömel, H., Naebert, T., Dirksen, R., and Sommer, M.: An update on the uncertainties of water vapor
36 measurements using Cryogenic Frostpoint Hygrometers, *Atmos. Meas. Tech.*, 9, 3755-3768,
37 <https://doi.org/10.5194/amt-9-3755-2016>, 2016.

38 Vogelmann, H., and Trickl, T.: Wide-range sounding of free-tropospheric water vapor with a differential-
39 absorption lidar (DIAL) at a high-altitude station, *Appl. Opt.*, 47, 2116-2132, 2008.

Irupdwlnhu#tejolv#k#huhlqlj#v#ljuhlfk,

1 Vogelmann, H., Sussmann, R., Trickl, T., and Borsdorff, T.: Intercomparison of atmospheric water vapor
2 soundings from the differential absorption lidar (DIAL) and the solar FTIR system on Mt. Zugspitze, *Atmos.*
3 *Meas. Tech.*, 4, 835-841, 2011.

4 Vogelmann, H., Sussmann, R., Trickl, T., and Reichardt, A.: Spatiotemporal variability of water vapor
5 investigated using lidar and FTIR vertical soundings above the Zugspitze, *Atmos. Chem. Phys.*, 14, 3135-3148,
6 2015.

7 Weinstock, E. M., Schwab, J. J., Nee, J. B., Schwab, M. J., and Anderson, J. G.: A cryogenically cooled
8 photofragment fluorescence instrument for measuring stratospheric water vapor”, *Rev. Sci. Instrum.*, 61, 1413-
9 1432, 1990.

10 Westwater, E. R.: The accuracy of water vapor and cloud liquid determination by dual-frequency ground-based
11 microwave radiometry”, *Radio Sci.*, 13, 677-685, 1978.

12 Whiteman, D. N., Rush, K., Rabenhorst, S., Welch, W., Cadirola, M., McIntire, G., Russo, F., Adam, M.,
13 Venable, D., Connell, R., Veselovski, I., Forno, R., Mielke, B., Stein, B., Leblanc, T., McDermid, S., and
14 Vömel, H.: Airborne and Ground-based measurements using a High-Performance Raman Lidar, *J. Atmos.*
15 *Ocean. Technol.*, 27, 1781–1801, 2010.

16 Whiteman, D. N., Venable, D., and Landulfo, E.: Comments on “Accuracy of Raman lidar water vapor
17 calibration and its applicability to long-term measurements”, *Appl. Opt.*, 50, 2170-2176, 2011.

18 Wing, R., Hauchecorne, A., Keckhut, P., Godin-Beekmann, S., Khaykin, S., McCullough, E. M., Mariscal, J.-F.
19 and d’Almeida, E.: Lidar temperature series in the middle atmosphere as a reference data set – Part I: Improved
20 retrievals and a 20-year cross-validation of two co-located French lidars, *Atmos. Meas. Tech.*, 11, 5531–5547,
21 2018.

22 Yoshino, K., Esmond, J. R., Parkinson, W. H., Ito, K., and Matsui, T.: Absorption cross section measurements of
23 water vapor in the wavelength region 120 to 188 nm, *Chem. Phys.*, 211, 387-391, 1996; erratum: *Chem. Phys.*,
24 215, 429-430, 1997.

25 Zahn, A., Christner, E., van Velthoven, P. F. J., Rauthe-Schöch, A., and Brenninkmeijer, C. A. M.: Processes
26 controlling water vapor in the upper troposphere/lowermost stratosphere: An analysis of 8 years of monthly
27 measurements by the IAGOS-CARIBIC observatory, *J. Geophys. Res.*, 119, 11505-11525, doi:
28 10.1002/2014JD021687, 2014.

29 Zöger, M., Afchine, A., Eicke, N., Gerhards, M.-T., Klein, E., McKenna, D. S., Mörschel, U., Schmidt, U., Tan,
30 V., Tuijter, F., Woyke, T., and Schiller, C.: Fast in situ stratospheric hygrometers: A new family of balloon-
31 borne and airborne Lyman- α photofragment fluorescence hygrometers, *J. Geophys. Res.*, 104, 1807-1816, 1999.

32

1 **Table 1. Transmitter Details**

2	Laser source	XeCl laser (Coherent, model Lambda SX)
3	Laser wavelength	307.955 nm
4	Maximum power (at 2.0 kV)	420 W
5	Stabilized power (all lines)	350 W
6	Single-line power	180 W
7	Line width	0.036 nm
8	Optimum spectral purity	99.5 %
9	Linear polarization	99.6 %
10	Pulse repetition rate	350 s ⁻¹
11	Raman shifted wavelength	353.144 nm
12	Maximum Raman conversion effi-	
13	ciency (f = 2.0 m, 40 bar, 350 s ⁻¹)	5 % with distorted alignment, otherwise 0 %
14	Second laser (starting 2018)	Nd:YAG (Continuum, model PL8020 Precision)
15	Wavelength	354.8123 nm (injection-seeded)
16	Pulse energy	160 mJ at 20 Hz repetition rate
17	Final beam expansion (f = 1.75 m)	5.7:1
18	Final beam dimensions	0.20×0.20 m ²
19	Final beam divergence	≤ 0.5 mrad

20
21

1	Table 2: Receiver Detailsdetails	
2	Primary mirrors	0.13 m diameter, $f = 0.72$ m
3		0.50 m diameter, $f = 2.0$ m
4	Field of view	large telescope: about 0.8×0.2 mrad ²
5	Detection wavelengths:	306.791 nm, 307.390 nm, 307.355 nm, 331.751 nm, 346.978 nm,
6		353.144 nm, 354.812336 nm ^a
7	Raman shifts:	Vibrational Q branch of H ₂ O ^b : 3652 cm ⁻¹ (centre of the stronger lines. Range
8		of Q-branch: 3628 to 3658 cm ⁻¹ ($\Delta\lambda = 0.36$ -nm)
9		nitrogen, Q ₆ line (population peak) ^c : 2329.1821 cm ⁻¹
10		N ₂ and O ₂ rotational shifts: taken from references in footnotes c and d
11		hydrogen, Q ₁ line ^e : 4155.2521 cm ⁻¹
12	Wavelength separation	polarization-sensitive beam splitters and interference filters
13		($\Delta\lambda = 0.75$ nm f.w.h.m. for H ₂ O, 0.25 nm otherwise)
14	PMTs	Hamamatsu R7400U-03, modified by RSV
15	Pre-amplifiers	Analog Modules, gain 1–10, bandwidth 4 MHz, sometimes used for H ₂ O
16	Transient digitizers	Licel, 6 units, 12 bit, 20 MHz, ground-free input stages
17	Photon counting	FAST ComTec, 100 ps time bins, 7.5-m detection bins

18
19 (a) Measured during the project described by Vogelmann and Trickl (2008)

20 (b) Avila et al., 2004

21 (c) Trickl et al., 1993; 1995

22 (d) Rouillé, 1992; Golubiatnikov and Krupnov, 2004

23 (e) Bragg et al., 1982; Dickensen et al., 2013

24

25

1 **Table 3: Specifications of the Polychromator-polychromator Optics**

2 **Broadband Optics**

3 Component	4 Diameter	5 Focal Length or Wavelength	6 Comments
7 f ₁ lenses	75 mm	150 mm	
8 f ₂ lenses	- <u>** 15 mm</u> <u>... ** 15 mm</u>	17 mm 30 mm	large telescope small telescope
9 45°-high reflectors	75 mm	all wavelengths	S and P polarization
10 45°-beam splitter 1	75 mm	308 nm	T = 99 % P (308 nm), T = 99-100 % P (> 325 nm) T = 94 % S (355 nm) R ≈ 99.8 % S (308 nm)
13 45°-beam splitter 2	75 mm	308 nm	T = 63 % S, R = 37 % S
14 45°-beam splitter 3	75 mm	308 nm	R = 100 % P (308 nm) T = 83 % P (332 nm)
16 45°-beam splitter 4	75 mm	355 nm	T ≈ 90 % P (347, 355 nm) T = 99 % P (332, 347 nm) R ≈ 99.8 % S (355 nm)
18 45°-beam splitter 5	75 mm	332 nm	R = 99.8 % P, T > 99 % P (347, 355 nm)
20 45°-beam splitter 6 ^{*)}	75 mm	347 nm	R = 84 % P T = 99.3 % P (353 nm)

23 ^{*)}No longer used since 2018, not shown in Fig. 9

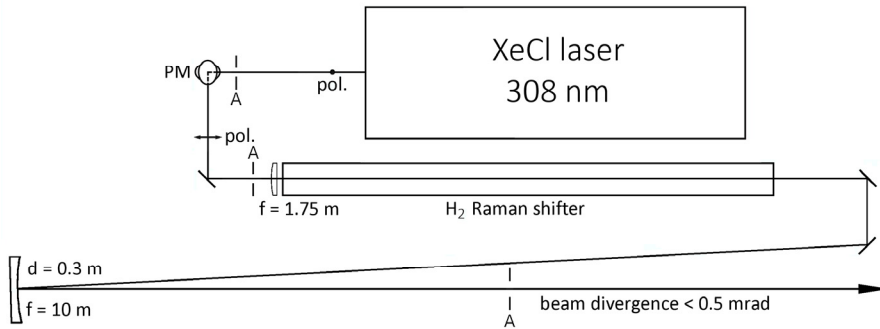
24 **Narrow-band Interference Filters**

26 Wavelength [nm]	27 Bandwidth [nm]	28 Maximum T (large telescope)	29 Maximum T (small telescope)	30 Producer
31 306.791	0.25	25 %	25 %	Materion Barr
32 307.390	0.15	27 %	25 %	Materion Barr
33 307.955	0.25	35 %	32 %	Materion Barr
34 331.7510.25	52 %	43 %	Materion Barr
35 346.978	0.75	74 %	62 %	Materion Barr
36 353.144	0.25	43 %	34 %	Materion Barr
37 354.812	< 1.2	> 80 %		Alluxa

35 All diameters 50 mm

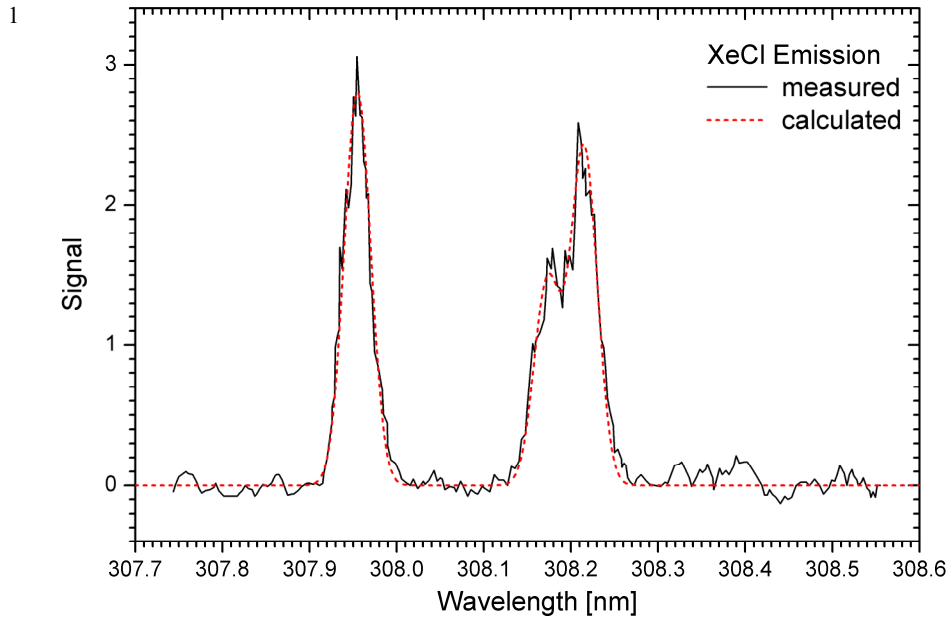
1 **Figures:**

2



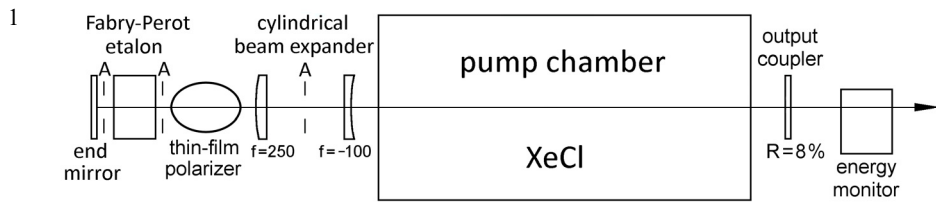
3 **Fig. 1.** Overview of the transmitter part of the UFS Raman lidar: The laser beam profile is expanded to a 36×36-
4 mm² square shape by a $f = -100\text{ mm} - f = 250\text{ mm}$ pair of cylindrical lenses (recently removed), sent down by a
5 combination of two plane mirrors (rotating the polarization by 90°) before it is focussed into a **high-pressure**
6 **vacuum cell (originally Raman shifter)** 3.6 m long with a $f = 1.75\text{ m}$ lens (initially $f = 2.0\text{ m}$). The beam diverges
7 from the focal point is **made-parallel-collimated** by an $f = 10\text{ m}$ concave mirror (**about $180 \times 180\text{ mm}^2$**) and
8 reaches the motorized beam-steering mirror in a vertical exit shaft outside the laboratory (not shown). Three
9 apertures (**A; 40 mm slit, $40 \times 40\text{ mm}^2$ square and $(w = 200) \times (h = 120)\text{ mm}^2$**) made of **sand-blasted-anodized**
10 **aluminium** allow to control the beam pointing **that can change during warm-up**.

11



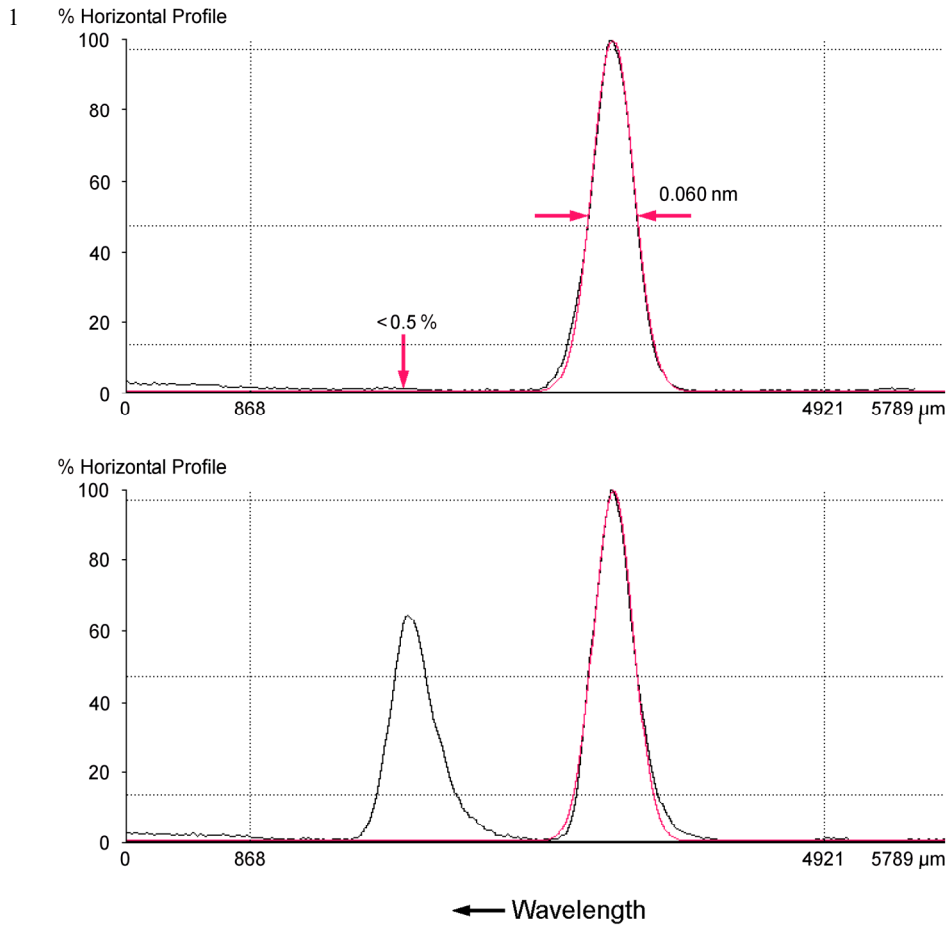
2 **Fig. 2.** Emission spectrum of a Coherent high-power XeCl laser in broadband operation (source: Coherent); the
3 dashed red curve is the sum of three Gaussian lines with centres at 308.955 nm, 308.173 nm and 308.215 nm and
4 full width at half maximum of 0.0357 nm.

5



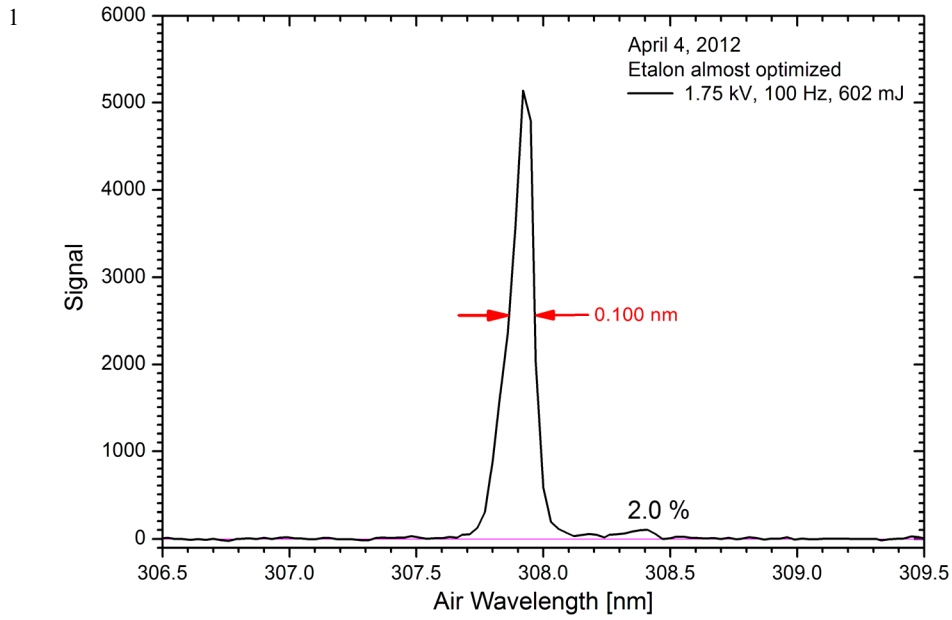
2 **Fig. 3.** Top view of the modified Lambda SX laser system; $36 \times 36\text{-mm}^2$ square apertures (A) are used for
 3 protecting optical components from potential powerful reflections from accidentally rotated components. The
 4 polarizer is oriented out of plane at Brewster's angle.

5
 6



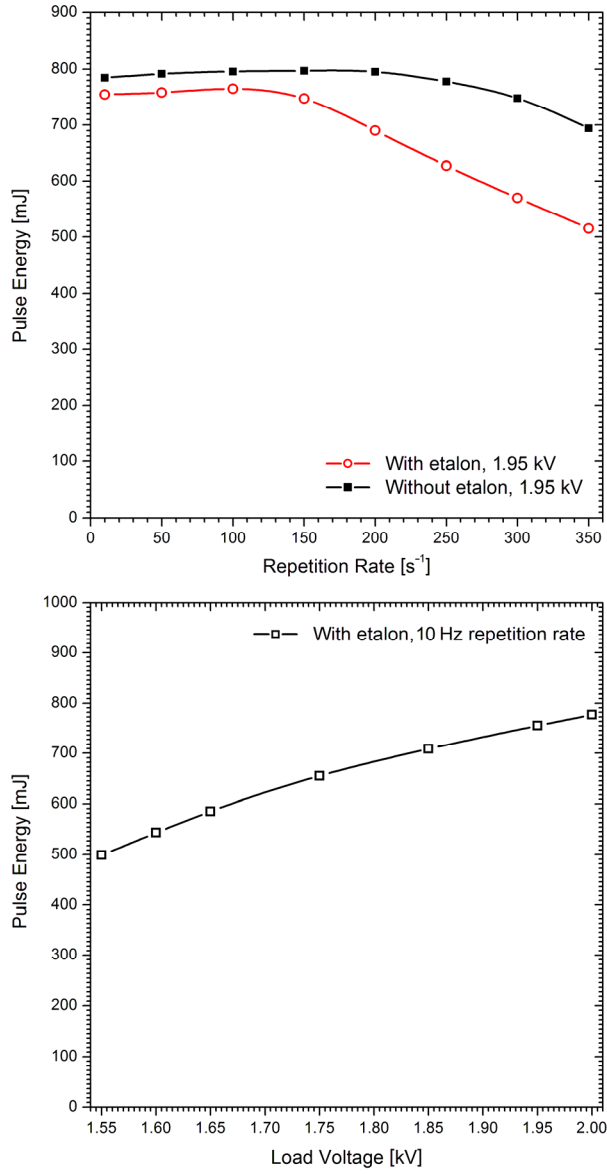
2 **Fig. 4.** Uncalibrated spectra of the laser emission with the laser running at 300 Hz (top) and 50 Hz (bottom,
 3 etalon removed); the red curves are Gaussian fits by the camera software. Asymmetries and the growing
 4 background towards higher wavelengths are to some extent ascribed to imperfections of the home-made
 5 spectrograph. The grid of the lower spectrum was slightly shifted to achieve position matching of the large peak
 6 (minor re-alignment of the spectrograph between the measurements)

7



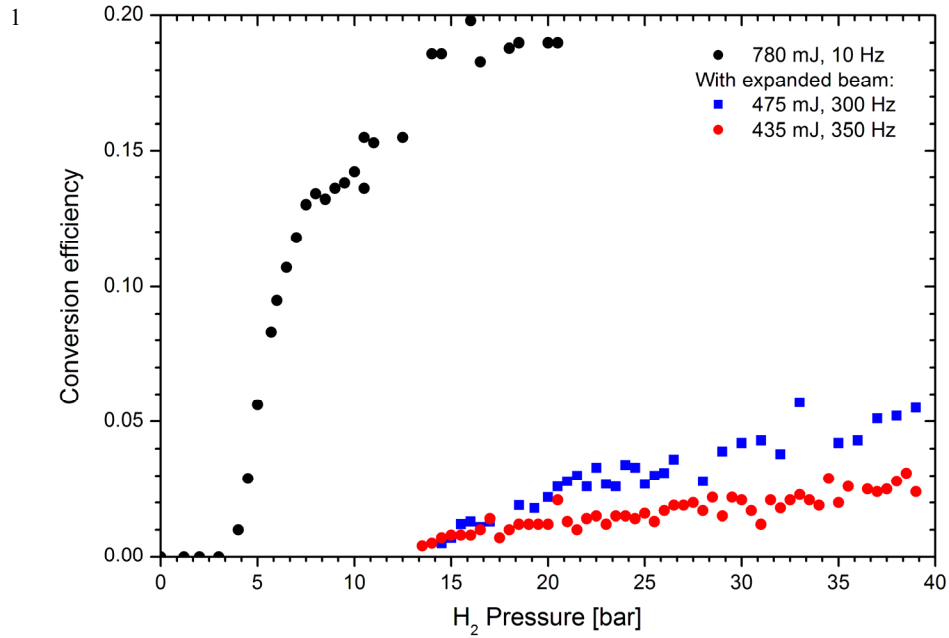
2 **Fig. 54.** Spectrum of the laser emission with almost optimized etalon angle; the laser was operated with 10 Hz
3 repetition rate, 1.75 kV load voltage and 663 mJ (including the polarizer).
4

1



2 **Fig. 65.** Optimized pulse energy as a function of the repetition rate (top) and load voltage (bottom); for
3 comparison: The maximum pulse energy of the broadband laser as delivered is 1.25 J (at 2.0 kV and 300 Hz).

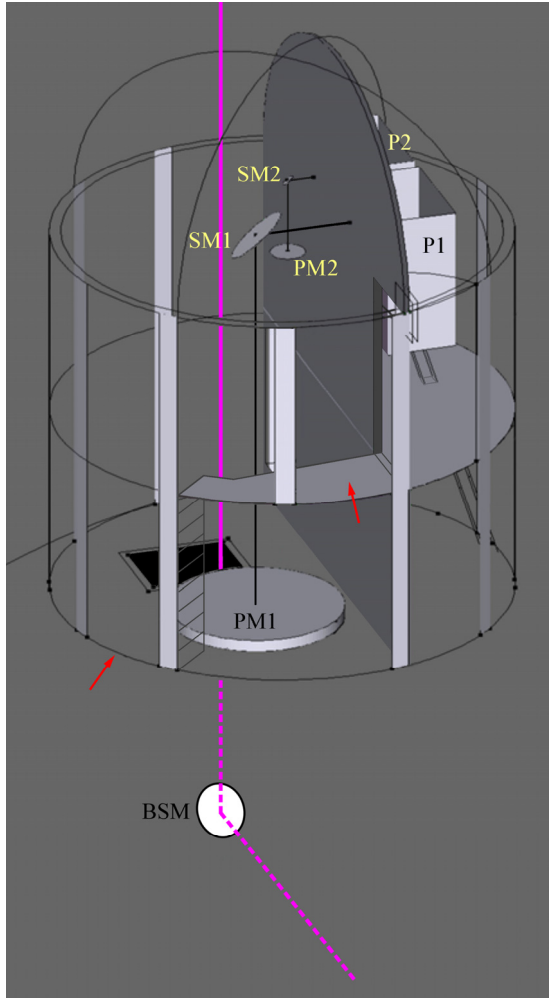
4
5



2 **Fig. 7.** Raman conversion efficiencies in hydrogen obtained for three different repetition rates ($f = 2.0$ m): The
 3 measurements at 10 s^{-1} repetition rate were made without etalon in the laser cavity, those at high repetition rates
 4 with all components installed.

5

1



2 **Fig. 86.** Receiver tower mounted on the terrace above the lidar laboratory: The tower is covered by a 4.2-m-
3 diameter astronomical dome with a 1.5-m slit: The laser beam (violet) emerges from a former emergency shaft.
4 The plane formed by the axes of the large telescope and the laser beam contains the section of the laser beam in
5 the lower floor. This plane is perpendicular to the plane formed by the axes of the small telescope and the laser
6 beam. Abbreviations:

7 BSM beam-steering mirror

8 PM: primary mirror

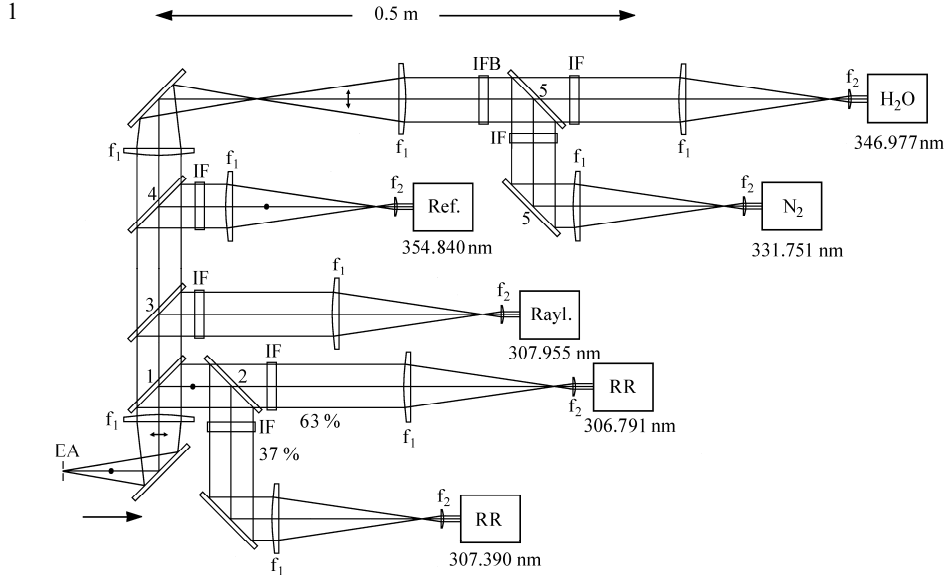
9 SM: secondary mirror

10 P: Polychromator

11 1, 2: belonging to far-field receiver, near-field-receiver, respectively

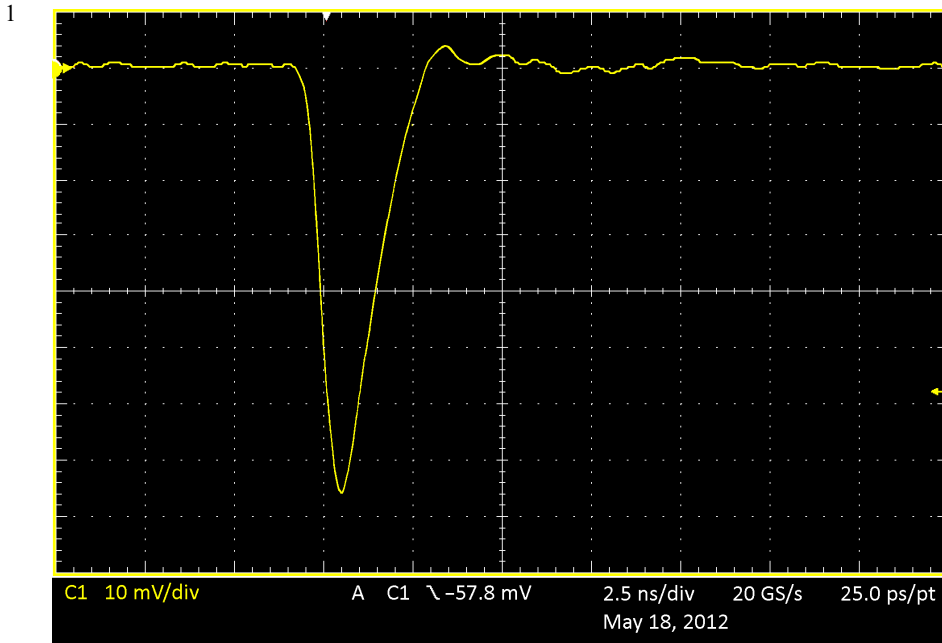
12 The two red arrows indicate the two entrances of the tower.

13



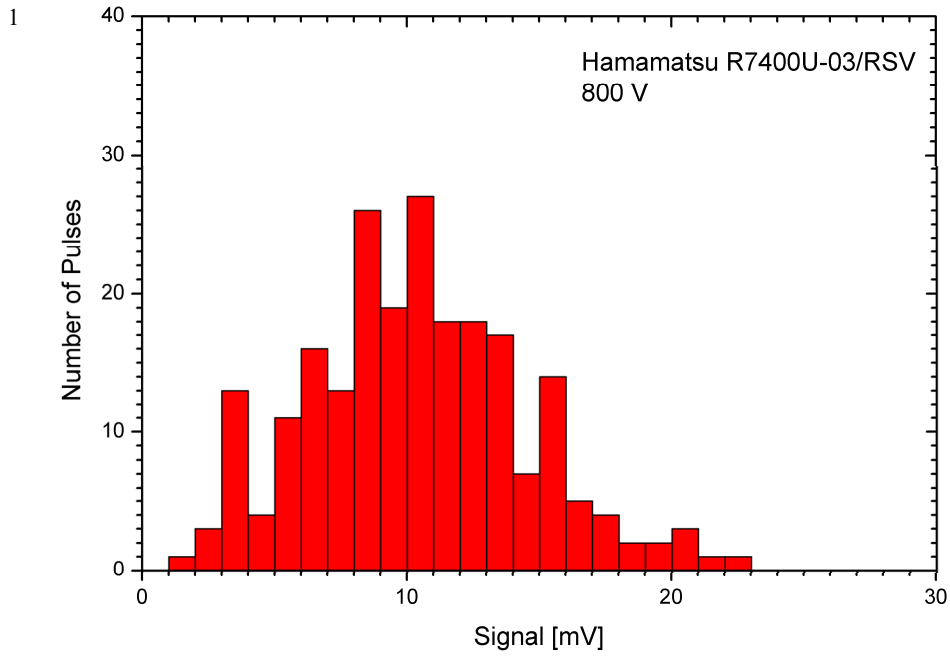
2 **Fig. 97.** Final polychromator design: The true orientation of the mounting plate (vertical) is rotated clockwise by
 3 90°. The radiation cone from the telescopes (arrow) enters the polychromators from behind the plate as indicated
 4 by the polarization dot next to the arrow. In detail:

- 5 EA: Entrance aperture with four adjustable blades (OWIS)
 6 1: Beam splitter transmitting almost all P-polarized radiation (308-355 nm) and highly reflects the S-
 7 polarized 308-nm radiation (Laseroptik)
 8 2: 63%/37% beam splitter for S-polarized 308-nm radiation (Laseroptik)
 9 3: Beam splitter reflecting all radiation at 308 nm and transmitting 83-91% of the longer-wavelength P
 10 components (Laseroptik)
 11 4: Polarizing beam splitter (Laseroptik)
 12 5: Sharp-edged long-pass filter for P polarization reflecting about 99% at 332 nm and transmitting 99%
 13 of the longer-wavelength components (Materion-Barr)
 14 IF: Interference filters with bandwidths of 0.25 nm except for 307.39 nm (0.15 nm) and 347 nm (0.75 nm)
 15 (Materion Barr, Alluxa)
 16 IBF: Broadband interference filter transmitting between 330 and 355 nm with $T = 85-90\%$ and blocking the
 17 radiation outside this range by at least 10^5 (Semrock).
 18 Lenses: $f_1 = 150$ mm and $f_2 = 18$ mm (large telescope), $f_2 = 30$ mm (small telescope)
 19 Detailed specifications: Table 3
 20
 21

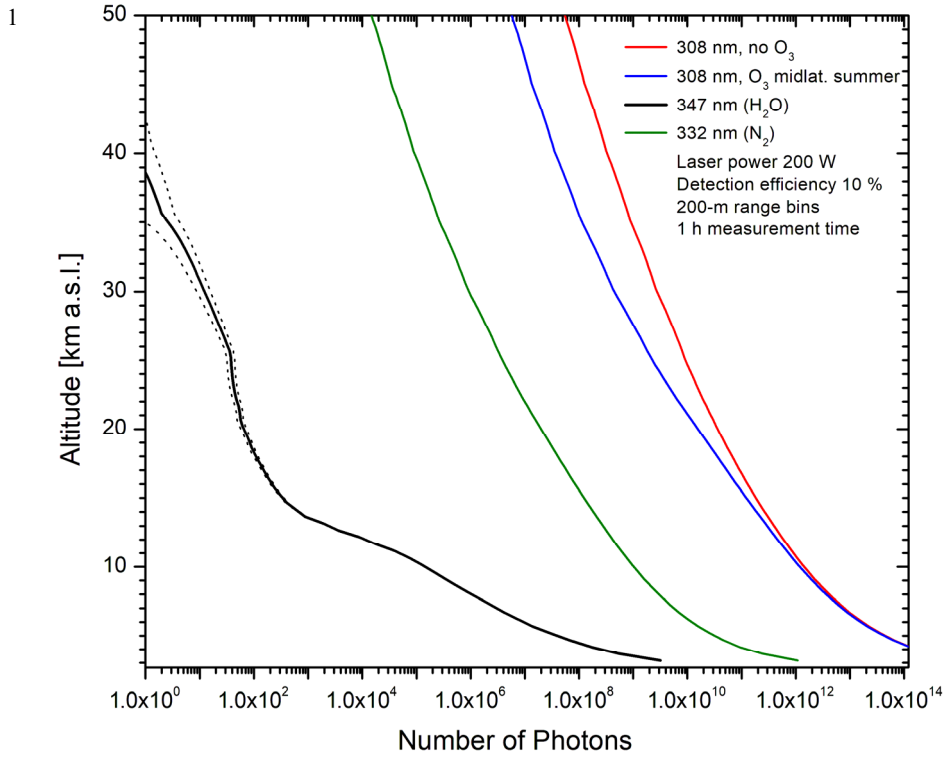


2 **Fig. 108.** Single-photon pulse from a Hamamatsu R7400P-03 PMT with the most recent version of the
3 Romanski (RSV) socket, measured with a 1-GHz digital oscilloscope (Tektronix, DPO 7104); from (Trickl et al.,
4 2020b)

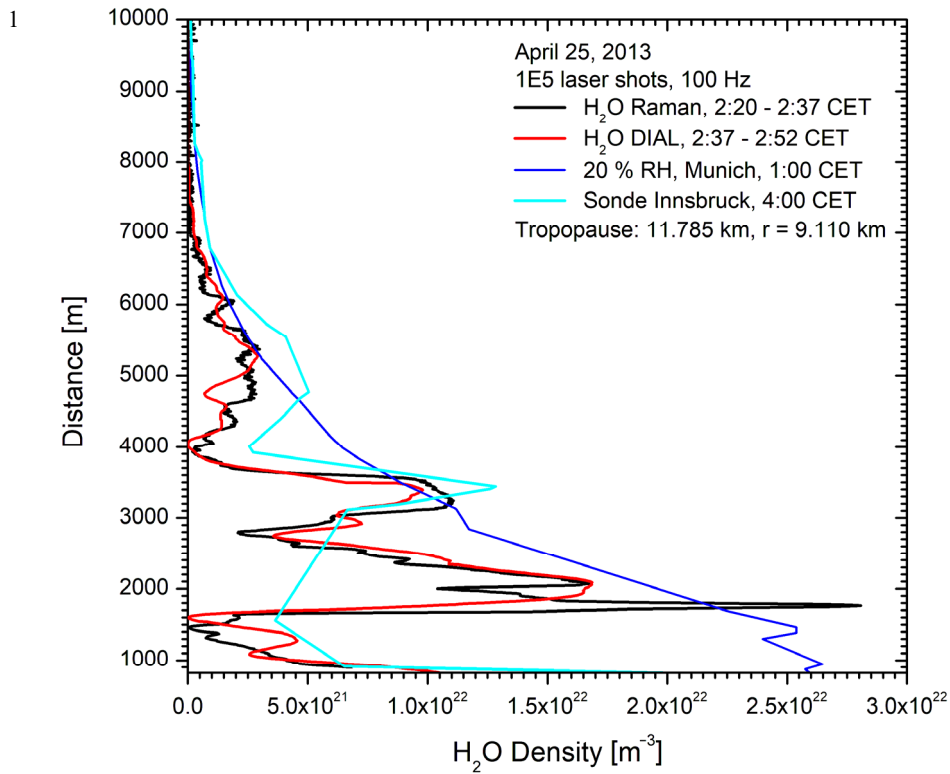
5



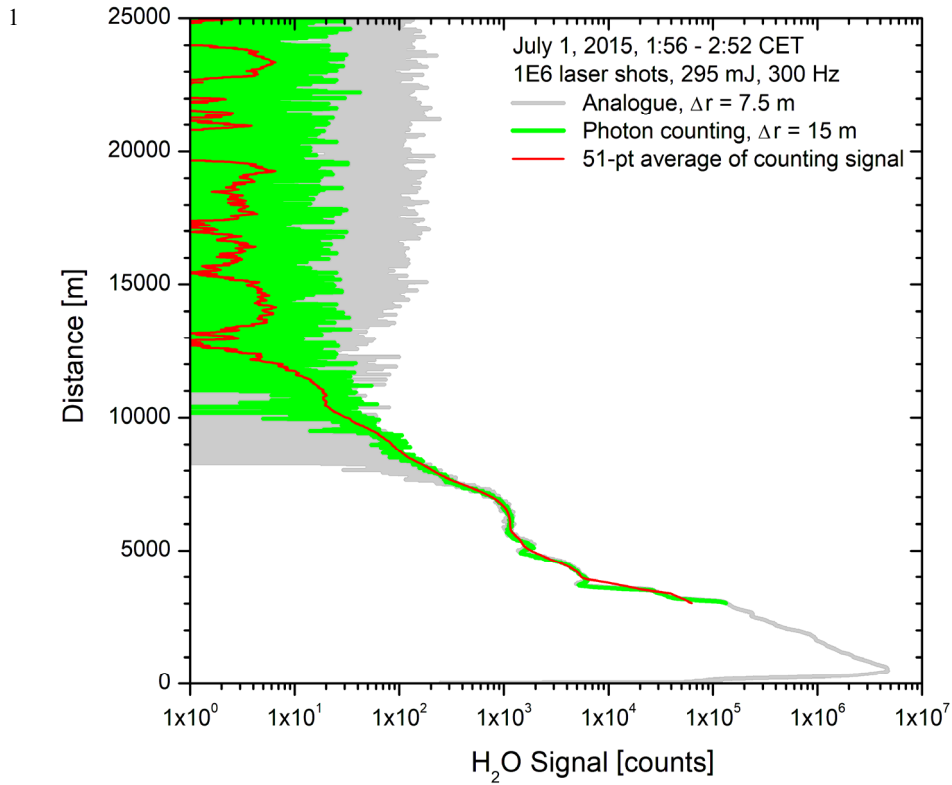
2 **Fig. 149.** Pulse height distribution of a Hamamatsu R7400-03 PMT (RSV module) for 800 V of operating
 3 voltage determined from a long time scan with a 1-GHz digital oscilloscope (sign of the pulse amplitudes
 4 inverted); from (Trickl, 2020b).
 5



2 **Fig. 4210.** Simulations of the backscatter signals for four wavelengths specified in the upper right corner; An
 3 average laser power at 308 nm of 200 W, a detection efficiency of 10 %, a range bin of 200 m and a
 4 measurement time of 1 h were assumed.
 5

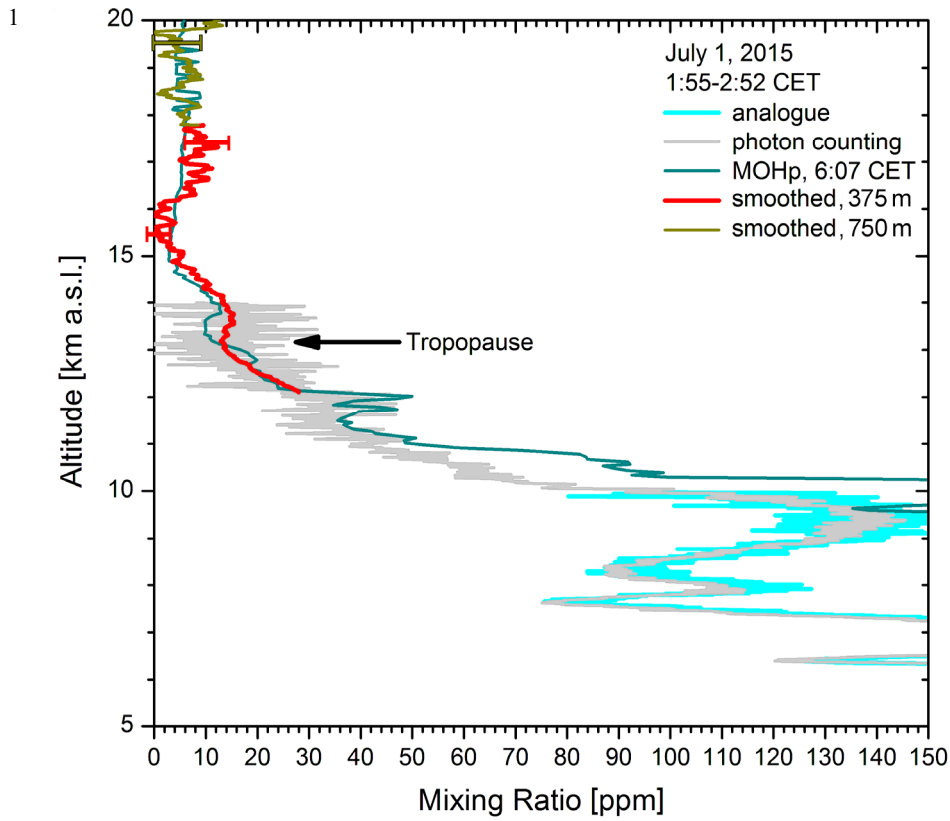


2 **Fig. 1311.** Comparison of consecutive measurements of the Raman lidar and DIAL at UFS on 25 April, 2013:
 3 the sonde measurements at Munich (not shown) and Innsbruck strongly differ from those of the lidar systems.
 4 For comparison, we show the densities corresponding to 20 % RH as calculated from the Munich radiosonde.
 5
 6



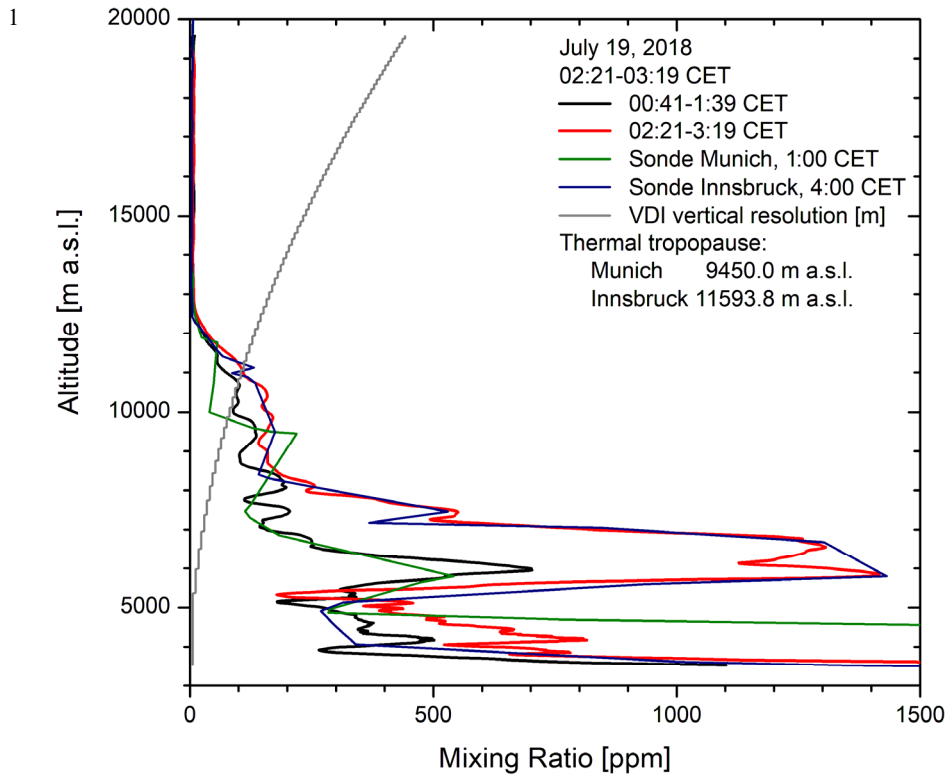
2 **Fig. 1412.** 347-nm Raman backscatter signals as a function of the vertical distance above UFS, obtained during
 3 the first hours on 1 July, 2015. Despite a high noise level of about 12 counts (square root of signal) the averaged
 4 signal remains positive up to $r = 19.7$ km. The averaged signal covers six decades, the peak signal being roughly
 5 3 mV. The average laser pulse energy, 295 mJ, was low due to a contaminated cell window.

6
 7

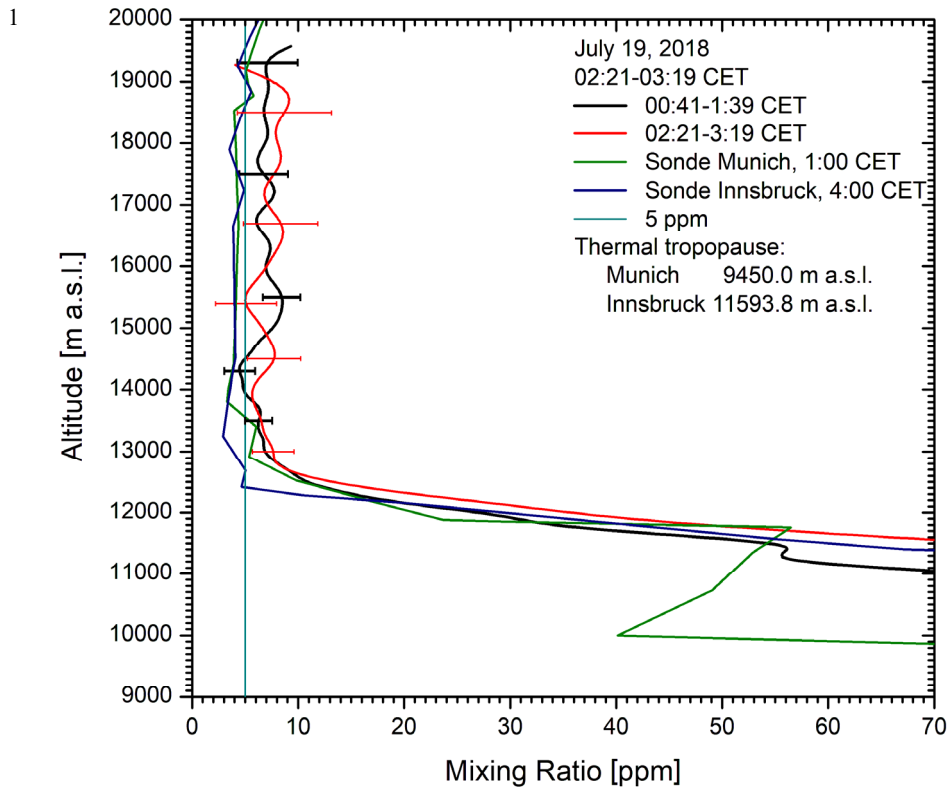


2 **Fig. 4513.** Water-vapour mixing ratio obtained for the measurement in Fig. 15; the calibration is based on
 3 looking at zones of best agreement below 7 km between the sonde data for Munich (1 CET), Innsbruck (4 CET)
 4 and Hohenpeißenberg (6 CET). Just the Hohenpeißenberg (MOHp) results are displayed here because they agree
 5 best with the lidar values above 11 km. 51-pt and 101-pt arithmetic-means smoothing was applied to the mixing
 6 ratios derived from the photon-counting data at high altitudes, the corresponding VDI vertical resolutions are
 7 specified in the legend.

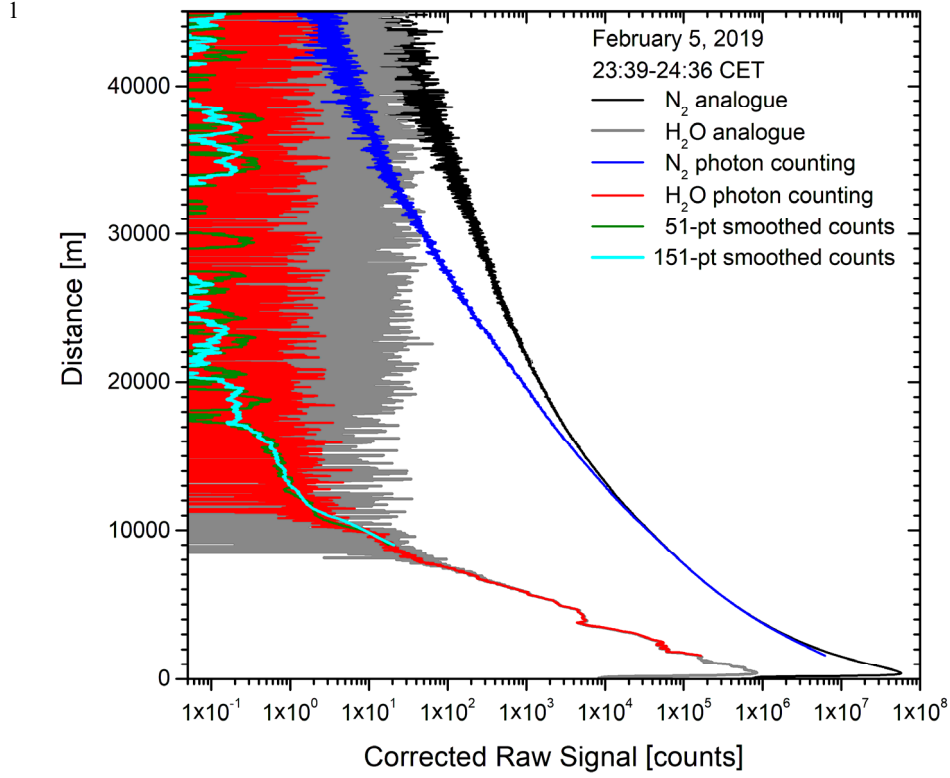
8



2 **Fig. 4614.** Calibration of the measurements on 19 July 2018: The profile derived from the first measurement
 3 agrees better with the 1:00 CET sonde data from Munich. The mixing ratios for the second measurement almost
 4 coincides with those from the later sonde launch at the airport of Innsbruck. The average laser pulse energy was
 5 380 mJ (300 Hz).
 6

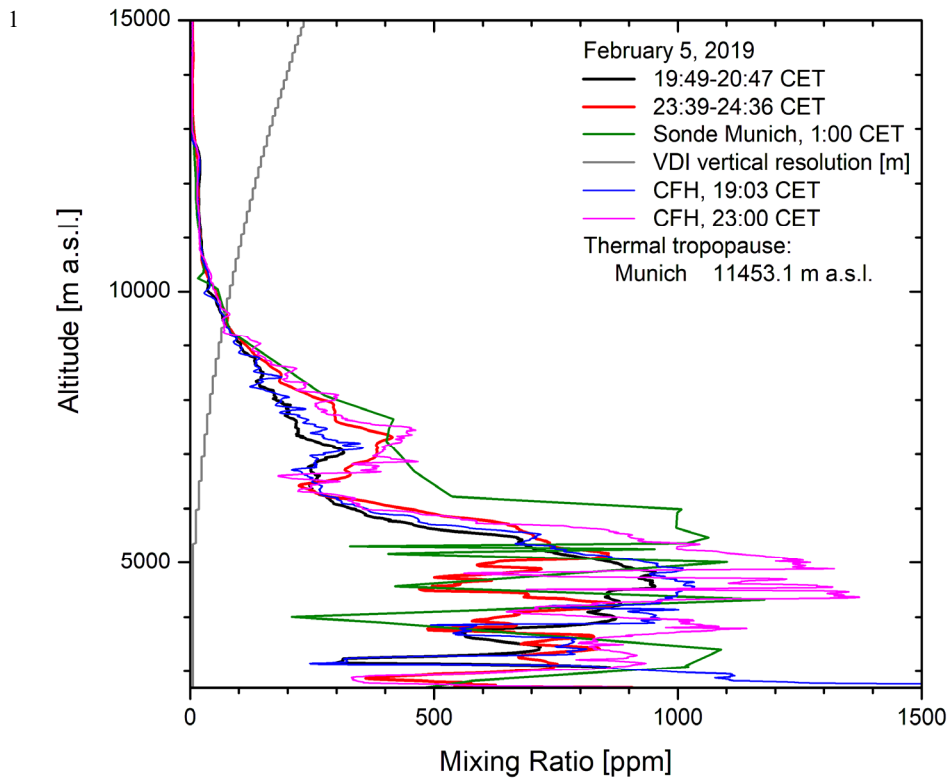


2 **Fig. 4715.** Comparison of the two lidar measurements on 19 July, 2018, and the Innsbruck sonde on a zoomed
 3 scale: The lidar values agree well up to 18 km, ranging between 5 ppm and 12 ppm. The mixing ratio for the
 4 radiosondes (presumably RS41) is much lower than that for the lidar in the stratosphere.
 5



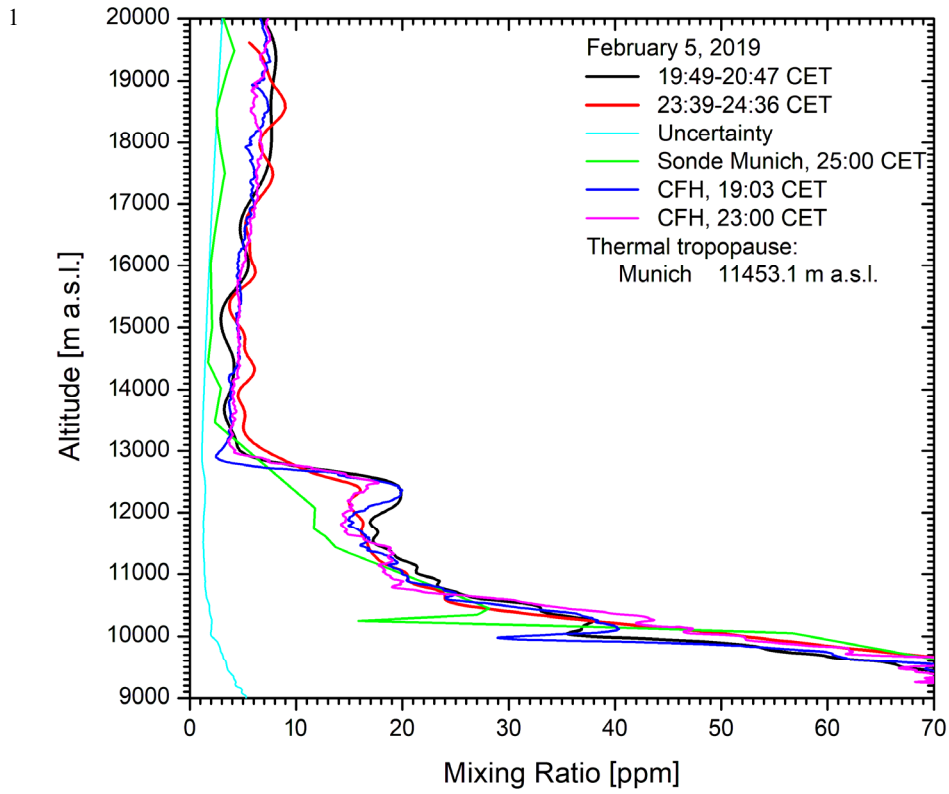
2 **Fig. 1816.** Nitrogen and water-vapour backscatter signals on 5 February 2019 as a function of the vertical
 3 distance above UFS; The H₂O backscatter profiles averaged over 151 7.5-m bins (i.e., raw data; VDI vertical
 4 resolution: 562.5 m) become noisy at about 17 km (19.7 km a.s.l.). The laser pulse energy was just 360 mJ (300
 5 Hz).

6
7
8
9
10

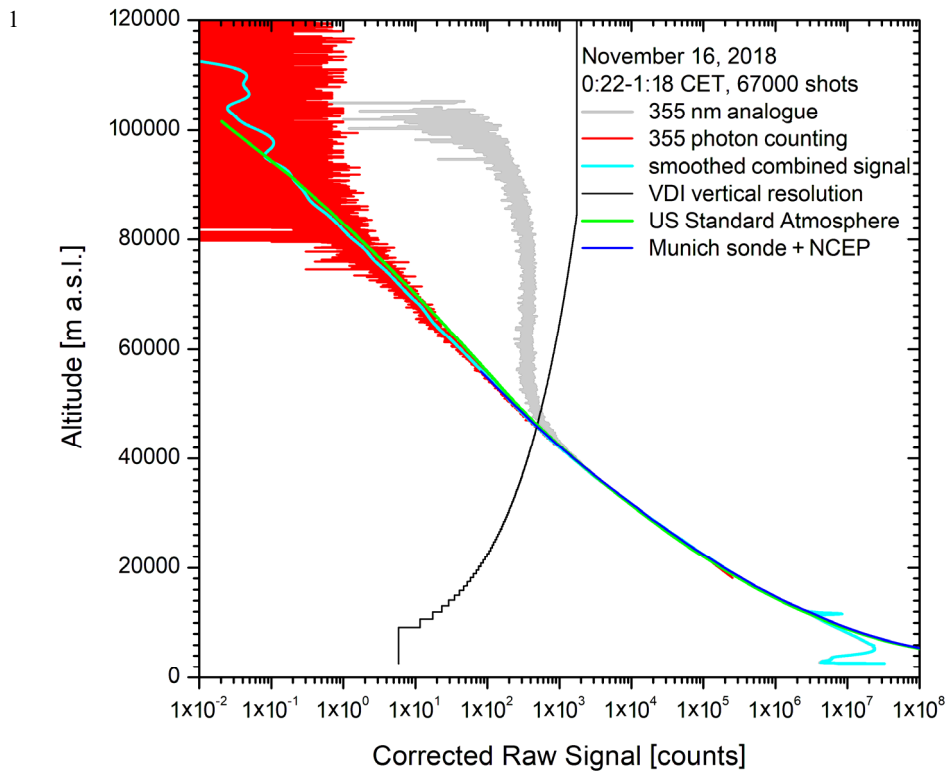


2 **Fig. 1917.** Vertical distributions of water-vapour derived from two measurements of the Raman lidar on 5
 3 February 2019 together with those from the midnight Munich sonde and the CFH sensors; the CFH data in the
 4 upper troposphere were used for calibration.

5

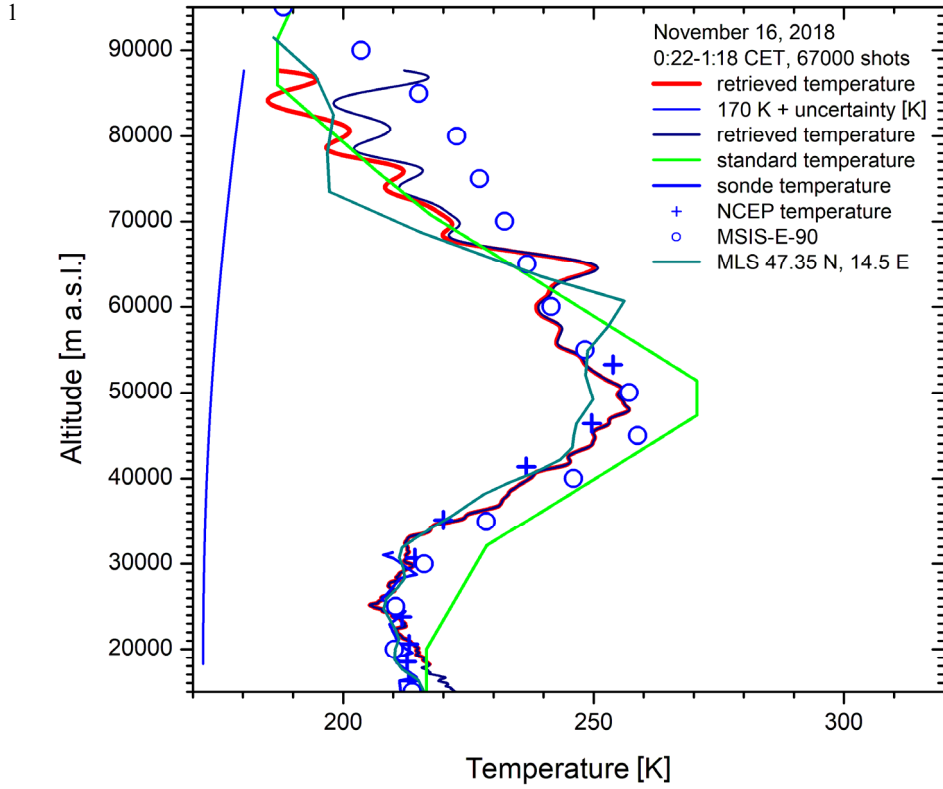


2 **Fig. 2018.** Zoomed portion of Fig. 20: The agreement between lidar and CFH is satisfactory up to almost 20 km.
 3 Above this, the lidar values start wider excursions around the CFH mixing ratios.
 4
 5



2 **Fig. 2419.** 355-nm backscatter coefficients for a 355-nm measurement on November 16, 2018: together with the smoothed signal combined analogue plus photon counting signal, shows low noise up to almost 95 km, corresponding to more than 8 decades of signal; the VDI vertical resolution of the smoothing procedure is given in metres. A simulated backscatter signal based on the U.S. Standard Atmosphere shows principal agreement, but there are some deviations. The agreement with the calculation calculated for from the U.S. Standard Atmosphere (1976) a combined radiosonde and NCEP profile is almost perfect up to the NCEP upper boundary of 50 km. They are included for comparison. NCEP-based profile was extrapolated to about 100 km. The VDI vertical resolution is given in metres.

10



2 **Fig. 2220.** Temperature profile from the measurement in Fig. 21, in comparison with data from the Munich 1:00
 3 CET radiosonde, NCEP (13:00 CET), the MSIS model and MLS; the temperatures were retrieved from the lidar
 4 signal by initializing the temperature at about 87 km using both the U.S. Standard and the MSIS values. Both
 5 retrievals converge to the same curve within 15-20 km from the top.